Ocean Engineering 37: 365–377, 2010

A nonlinear PDE formulation for offshore vessel pipeline installation

Gullik A. Jensen [a,b], Niklas Säfström [c], Tu Duc Nguyen [a,d], Thor I. Fossen [a,b]

[a] Department of Engineering Cybernetics, Norwegian University of Science and Technology, NO-7491 Trondheim, Norway
[b] Centre for Ships and Ocean Structures, Norwegian University of Science and Technology, NO-7491 Trondheim, Norway
[c] Department of Mathematical Sciences, Norwegian University of Science and Technology, NO-7491 Trondheim, Norway
[d] Siemens Oil and Gas Offshore, NO-7037 Trondheim, Norway

A B S T R A C T

In this paper a nonlinear dynamic PDE formulation for a pipe string suspended from a pipelay vessel to the seabed in a pipelay operation is developed. This model extends a three-dimensional beam model capable of undergoing finite extension, shearing, twist and bending, to apply for marine applications by adding the effects of restoring forces, hydrodynamic drag and seabed interaction. The model is validated against the natural catenary equation and the FEM code RIFLEX. The model is extended to include the pipelay vessel dynamics by applying a potential theory formulation of a surface vessel, suited for dynamic positioning and low speed maneuvering, as a boundary condition for the PDE. This system is found to be input–output passive and stable. Pipeline installation applications where the presented model is suited are e.g., analysis and simulation of the installation operation, operability analysis, hardware-in-the-loop (HIL) testing for vessel control systems, and automation of the pipelay operation.

1. Introduction

Slender marine structures are characterized by having a small cross-section area compared to the overall structure length, and in the offshore industry these structures have many applications, such as mooring lines, umbilicals, towers, pipelines and risers, e.g., drilling risers, production risers, export risers and workover risers. Having a good understanding of the dynamics of such structures is important for marine applications, and this understanding can be acquired from simulations based on mathematical models.

In this paper offshore pipeline installation from a surface vessel, a so-called *pipelay operation*, is considered, see Fig. 1, where the main objective of the operation is to position a pipeline along a predefined path on the seabed from the vessel, only by means of active control of the pipelay vessel position, while at all times ensuring the structural integrity of the pipe (Jensen et al., 2009a). The different methods used in pipelay operations are well described in recent textbooks on pipelaying, e.g., Braestrup et al. (2005), Guo et al. (2005) and Palmer and King (2008), while the present trends in deepwater pipelay systems in general are well described by Heerema (2005) and the references therein.

1.1. Pipeline modeling

In the design phase of an offshore pipeline project, mathematical models for the pipeline dynamics are needed to determine pipe properties, pipelay parameters, and the conditions under which the pipeline can safely be installed. Offshore pipelay operations were first conducted in shallow waters close to shore, where the strains and stresses in the pipe could satisfactorily be approximated by analytic models, such as the catenary equation known from cable mechanics (Irvine, 1981), and the stiffened catenary equation (Plunkett, 1967; Dixon and Rutledge, 1968). As pipelay operations were taken into deeper waters the dynamic behavior of the pipe became significant. Hence, dynamic pipe models based on elastic beam models, known from continuum mechanics, were introduced. These models were discretized, using e.g., the finite element method or the finite difference method (FEM), and solved numerically using computers.

Today, computer codes based on FEM, e.g., RIFLEX, ABAQUS, OFFPIPE and SIMLA, are the method of choice for analysis and simulation of pipelay operations, since these computer codes produce high quality discrete dynamic models. A case-study using ABAQUS is found in Martinsen (1998).

In this paper a nonlinear model for pipe string dynamics is developed by extending a finite strain beam formulation, which is three-dimensional and capable of undergoing finite extension, shearing, twisting and bending, first presented in Simo (1985). The principle of superposition (Faltinsen, 1990) is frequently applied in ocean engineering and is used to extend this model to

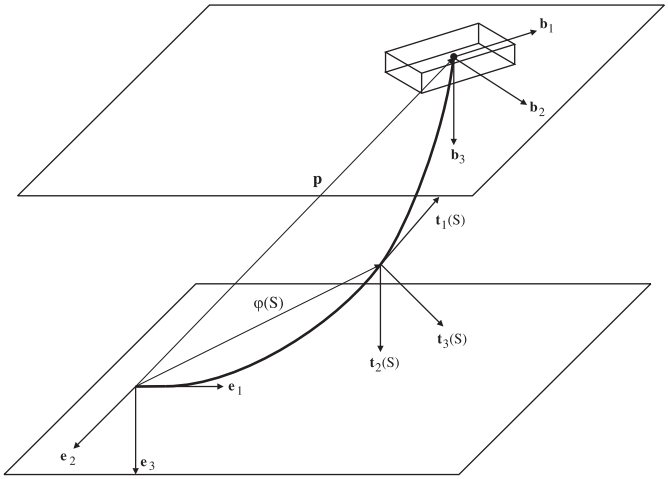

Fig. 1. Illustration of a J-lay installation in three dimensions with the three reference frames applied. The position of the pipelay vessel center of mass, illustrated by the box, is in the spatial frame $\boldsymbol{e}$ given by $\boldsymbol{p}$.

account for the effects of gravity and buoyancy as well as hydrodynamic drag and seabed interaction. This model is then semi-discretized in space, which yields a set of ordinary differential equations (ODEs), which can be applied in simulations of multibody systems, or in advanced controllers. An advantage of this model is that analyses can be performed directly on the continuous system, rather than on a discretized system. This model is then validated against the catenary equation and the commercial computer code RIFLEX (Fylling et al., 2008), which holds an international leading position in FEM analysis for slender marine structures.

A potential theory formulation of a surface vessel, suited for dynamic positioning and low speed maneuvering, is used as the upper boundary condition to form a system encompassing both pipe and vessel. Hence, analyses where the dynamics of the vessel is integrated can be performed with vessel control forces as the input. It seems plausible that a computer code for dynamic simulation based on this model may be lighter and faster compared to present alternatives, since the discretization and integration methods can be chosen based on detailed knowledge of the model, see e.g., Romero and Armero (2002), Betsch and Steinmann (2002) and McRobie and Lasenby (1999). However, the objective of this paper is limited to develop and validate the model. Applications related to pipeline installation are, e.g., simulation of the installation operation, operability analysis, hardware-in-the-loop (HIL) testing for vessel control systems, and pipelay operation automation. It seems also plausible that the model is not limited to pipelines, but is valid for many linearly elastic slender marine structures.

1.2. Automating pipelay operations

Today pipelay operations mostly rely on manually operated dynamic positioning (DP) systems for vessel positioning. Following Jensen et al. (2009a), it seems plausible that introducing automatic control systems can improve the performance in this industry, as it has for several other industries, including the process industry and the aerospace industry (Åström, 1996). Consequently, closed-loop automatic control for pipelay operations is a relatively new application which may now gain more attention as DP systems have become standard for deep-water pipelay operations.

The issue of stability of the closed-loop feedback system arises when FEM computer code models are considered for application in model-based controllers. Stability properties, such as passivity must be shown for the pipe model, and the potentially large number of states and equations may complicate this analysis. Furthermore, mechanical flexible systems are continuous with infinite degrees of freedom, so-called *infinite-dimensional*. In practice these systems are modeled as finite-dimensional with a large number of dimensions, and the fundamental problem of actively controlling such systems is to control the large-dimensional system with a much smaller dimensional controller. This issue was addressed by Balas (1978), who showed that such controllers can become unstable when connected to systems with infinite degrees of freedom even if the discrete model is shown to be passive. This is due to the unmodeled modes in the system, named *the spillover*, which the controller does not account for.

In this paper the passivity analysis of the pipe model is performed to show stability before the system is discretized by a finite element method. By careful discretization, this property can be preserved, and the closed-loop system will also be stable. This model feature indicates that it may be a suitable candidate for implementation in a model-based controller. The passivity analysis is extended to the complete system including the vessel as the upper boundary condition. This result is important in that a necessary property for implementing the model in model-based controllers is establishes.

2. Mathematical model

The model of the pipe dynamics is a partial differential equation (PDE) extending the nonlinear beam formulation developed and investigated by Simo et al. in a series of papers (Simo, 1985; Simo and Vu-Quoc, 1986, 1988; Simo et al., 1995). The formulation is a reparametrization of the formulation originally developed by Reissner (1982), where this model again can be regarded as a generalization of a three-dimensional extension of the classical Kirchhoff–Love rod model (Love, 1944). The extension includes finite extension and finite shearing of the rod. New to the model in this paper is the hydrodynamic and hydrostatic effects caused by the marine environment as well as the seabed interaction.

A vessel model in the time domain, suitable for low speed maneuvering and station keeping, is fixed to the surface end of the pipe string as the upper boundary condition. The vessel model is obtained by considering the forces and moments on a rigid body as well as hydrodynamic radiation forces and wave loads and the resulting state space model is a system of ordinary differential equations in the time domain.

In this section, the notation and reference frames are introduced, followed by the kinematics and the dynamics, including the boundary conditions.

2.1. Notation

Bold face lower and upper case letters denote vectors and matrices, respectively, and a superscript denote the reference frame of coordinate vectors. This may be omitted if the frame dependency is evident. With a small abuse of notation, the derivative with respect to time is denoted by a superposed dot and the derivative with respect to space, the curve parameter S, is denoted by a prefixed ∂_S. The usual inner product of $\boldsymbol{a}, \boldsymbol{b} \in \mathbb{R}^n$ is denoted $\langle \boldsymbol{a}, \boldsymbol{b} \rangle$ or equivalently on vectorial form $\boldsymbol{a}^{\mathrm{T}}\boldsymbol{b}$.

2.2. Reference frames

Three Cartesian reference frames denoted by $\boldsymbol{e}$, $\boldsymbol{t}$ and $\boldsymbol{b}$ are required in the development of the pipelay system model, see Fig. 1. Let $\boldsymbol{e}$ be an inertial frame with base $\boldsymbol{e}_1, \boldsymbol{e}_2, \boldsymbol{e}_3$, where the origin O_e is fixed to the seabed at $S = 0$. Let $\boldsymbol{t}(S)$ be a body-fixed frame with base $\boldsymbol{t}_1(S), \boldsymbol{t}_2(S), \boldsymbol{t}_3(S)$ and origin $O_t(S)$ located at the centroid of the pipe cross-section at S, where $S \in [0, L]$ is the spatial pipe variable, and L is the total length of the undeformed pipe. The base vector $\boldsymbol{t}_1(S)$ is directed normal to the cross-section plane, and $\boldsymbol{t}_2(S)$ and $\boldsymbol{t}_3(S)$ are directed along its principal axes. Let $\boldsymbol{b}$ be body-fixed with origin O_b at the pipelay vessel center of mass, with basis $\boldsymbol{b}_1, \boldsymbol{b}_2, \boldsymbol{b}_3$ along the principle axes of symmetry for the vessel, in accordance with (SNAME, 1950). The $\boldsymbol{e}$ and $\boldsymbol{t}$ frames are frequently referred to as the *spatial* and *material* frames, respectively.

The coordinate transformation of vectors from one frame to another is given by

$$\mathbf{v}^y = \boldsymbol{R}_x^y \mathbf{v}^x, \quad x, y \in \{\boldsymbol{e}, \boldsymbol{t}, \boldsymbol{b}\}, \quad \mathbf{v} \in \mathbb{R}^3, \tag{1}$$

where

$$\boldsymbol{R}_x^y \in SO(3), \quad SO(3) \triangleq \{\boldsymbol{R}_x^y \in \mathbb{R}^{3\times 3} | (\boldsymbol{R}_x^y)^{\mathrm{T}} \boldsymbol{R}_x^y = \boldsymbol{I}_{3\times 3}, \det \boldsymbol{R}_x^y = 1\}, \tag{2}$$

is a so-called *rotation matrix* from y to x, that transforms the vector coordinates of $\mathbf{v}$ in frame x to frame y. This notation is adopted from Egeland and Gravdahl (2002). In addition to representing the coordinate transformation between the coordinates of a point expressed in two different frames, the rotation matrix is also describing the mutual orientation between two coordinate frames where its column vectors are the directional cosines of the axes of the rotated frame with respect to the original frame (Sciavicco and Siciliano, 2001). Transformations between the defined frames $\boldsymbol{e}$, $\boldsymbol{t}$ and $\boldsymbol{b}$ are handled by the rotation matrices

$$\boldsymbol{R}_t^e(S), \boldsymbol{R}_b^e, \boldsymbol{R}_b^t \in SO(3), \tag{3}$$

where, e.g., $\boldsymbol{R}_t^e$ transforms coordinate vectors from in frame $\boldsymbol{t}$ to frame $\boldsymbol{e}$. Equivalent interpretations are given for $\boldsymbol{R}_b^e$ and $\boldsymbol{R}_b^t$ such that

$$\boldsymbol{t}_i^e(S) = \boldsymbol{R}_t^e(S) \boldsymbol{e}_i^e, \quad \boldsymbol{b}_i^e = \boldsymbol{R}_b^e \boldsymbol{e}_i^e, \quad \boldsymbol{b}_i^t = \boldsymbol{R}_b^t \boldsymbol{t}_i^t. \tag{4}$$

A rotation can be expressed as a sequence of partial rotations where each rotation is defined with respect to the preceding one (Sciavicco and Siciliano, 2001). Hence, a rotation matrix of composite rotations is the product of rotation matrices, and $\boldsymbol{R}_b^e$ can be found by the composite rotations

$$\boldsymbol{R}_b^e = \boldsymbol{R}_t^e(L) \boldsymbol{R}_b^t. \tag{5}$$

2.3. Model preliminaries

From a classical point of view the pipeline can be considered similar to a hollow rod, a three-dimensional slender body with uniform density and circular cross-sections. The reference configuration of the pipe is described by a smooth curve $\boldsymbol{\varphi}_r$, connecting the centroids of the cross-section planes, where the tangent of $\boldsymbol{\varphi}_r$ is normal to each cross-section, see Fig. 2. Any configuration of the pipe can then be given by a smooth curve $\boldsymbol{\varphi} : [0, L] \to \mathbb{R}^3$, the so-called *line of centroids*. The cross-sections are assumed to remain unchanged in shape while the pipe is undergoing motion. The assumption that the cross-sections remain normal to the tangent $\partial_S \boldsymbol{\varphi}$, known from the Euler–Bernoulli beam theory, is relaxed to account for shearing effects. The position of any point along the line of centroids is given by $\boldsymbol{\varphi}(S)$, and the orientation of the cross-section at $\boldsymbol{\varphi}(S)$ is given by $\boldsymbol{R}_t^e(S)$. Hence, the configurations of the pipe are completely defined

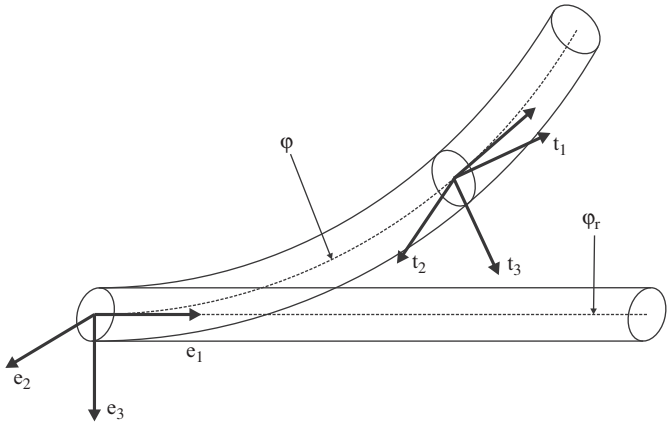

Fig. 2. The pipe configuration is given by the line of centroids $\boldsymbol{\phi}$, where the reference configuration is given as $\boldsymbol{\phi}_r$. The cross-section of the pipe at $\boldsymbol{\phi}(S)$ is spanned by $\boldsymbol{t}_2(S)$ and $\boldsymbol{t}_3(S)$.

by specifying $\boldsymbol{\varphi}(S, t)$ and $\boldsymbol{R}_t^e(S, t)$, where S is the curve parameter, and t is the time. The *configuration space* for the elastic pipe is given by

$$\mathcal{C} \triangleq \{(\boldsymbol{\varphi}, \boldsymbol{R}_t^e) | S \in [0, L] \to \mathbb{R}^3 \times SO(3) | \langle \partial_S \boldsymbol{\varphi}(S), \boldsymbol{R}_t^e \boldsymbol{e}_1^e \rangle > 0\}, \tag{6}$$

and the reference configuration is taken as $(\boldsymbol{\varphi}_r, \boldsymbol{R}_{t,r}^e) \in \mathcal{C}$ such that

$$\boldsymbol{\varphi}_r(S) = S\boldsymbol{e}_1^e, \quad \boldsymbol{R}_{t,r}^e(S) = \boldsymbol{I}_{3\times 3}. \tag{7}$$

2.4. Kinematics

The derivatives of $\boldsymbol{\varphi}(S, t)$ and $\boldsymbol{R}_t^e(S, t)$, the material stress resultant and stress couple are derived in this section.

2.4.1. Time and space derivatives

Differentiating (4) with respect to time t yields

$$\dot{\boldsymbol{t}}_i^e = \boldsymbol{S}(\mathbf{w}^e) \boldsymbol{t}_i^e, \quad \boldsymbol{S}(\mathbf{w}^e) = \dot{\boldsymbol{R}}_t^e (\boldsymbol{R}_t^e)^{\mathrm{T}}, \tag{8}$$

where $\boldsymbol{S}(\cdot) : \mathbb{R}^3 \to T_I SO(3)$, is the skew-symmetric map, defined as

$$\boldsymbol{S}(\mathbf{v}) \triangleq \begin{bmatrix} 0 & -v_3 & v_2 \\ v_3 & 0 & -v_1 \\ -v_2 & v_1 & 0 \end{bmatrix}, \quad \mathbf{v} \in \mathbb{R}^3. \tag{9}$$

The *spin* of the moving frame is defined as the skew-symmetric tensor $\boldsymbol{S}(\mathbf{w}^e(S, t))$, and the associated axial vector $\mathbf{w}^e(S, t)$ defines the *vorticity*. The time derivative of $\boldsymbol{R}_t^e$ is thus given by the two alternative forms

$$\dot{\boldsymbol{R}}_t^e = \boldsymbol{R}_t^e \boldsymbol{S}(\mathbf{w}^t), \tag{10}$$

$$\dot{\boldsymbol{R}}_t^e = \boldsymbol{S}(\mathbf{w}^e) \boldsymbol{R}_t^e. \tag{11}$$

The linear velocity vector is given in the spatial and material frames, respectively, as

$$\dot{\boldsymbol{\varphi}} \in \mathbb{R}^3, \quad \mathbf{v}^t = (\boldsymbol{R}_t^e)^{\mathrm{T}} \dot{\boldsymbol{\varphi}}, \tag{12}$$

where differentiating (12) yields the linear acceleration

$$\ddot{\boldsymbol{\varphi}} \in \mathbb{R}^3, \quad \dot{\mathbf{v}}^t = (\boldsymbol{R}_t^e)^{\mathrm{T}} \ddot{\boldsymbol{\varphi}} - (\boldsymbol{R}_t^e)^{\mathrm{T}} [\mathbf{w}^e \times \dot{\boldsymbol{\varphi}}]. \tag{13}$$

The space derivative of the position vector is simply denoted $\partial_S \boldsymbol{\varphi}(S, t) \in \mathbb{R}^3$, and the corresponding material derivative of $\boldsymbol{R}_t^e$ is, like the time derivative, obtained from (4). Hence,

$$\partial_S \boldsymbol{R}_t^e = \boldsymbol{R}_t^e \boldsymbol{S}(\boldsymbol{\omega}^t), \tag{14}$$

$$\partial_S \boldsymbol{R}_t^e = \boldsymbol{S}(\boldsymbol{\omega}^e) \boldsymbol{R}_t^e, \tag{15}$$

where $\boldsymbol{\omega}^t$ and $\boldsymbol{\omega}^e$ represents the curvature or bending in material and spatial form, respectively. Since derivation with respect to time and space are commutative operations, evaluating the identity

$$\partial_S(\partial_t \boldsymbol{R}_t^e) = \partial_t(\partial_S \boldsymbol{R}_t^e) \tag{16}$$

by taking the spatial derivative of (10) and the time derivative of (14), yields the following expression relating $\boldsymbol{\omega}$ and $\mathbf{w}$:

$$\dot{\boldsymbol{\omega}}^t = \partial_S \mathbf{w}^t + \boldsymbol{\omega}^t \times \mathbf{w}^t = (\boldsymbol{R}_t^e)^{\mathrm{T}}[\partial_S \mathbf{w}^e + \boldsymbol{\omega}^e \times \mathbf{w}^e]. \tag{17}$$

2.4.2. Stress

The material stress resultant $\boldsymbol{n}^t$ and stress couple $\boldsymbol{m}^t$ are obtained from the bilinear quadratic energy function $\boldsymbol{\Psi}(\boldsymbol{\gamma}^t, \boldsymbol{\omega}^t)$ (Simo, 1985):

$$\boldsymbol{n}^t = \frac{\partial}{\partial \boldsymbol{\gamma}^t}\boldsymbol{\Psi}, \quad \boldsymbol{m}^t = \frac{\partial}{\partial \boldsymbol{\omega}^t}\boldsymbol{\Psi}, \tag{18}$$

where

$$\boldsymbol{\Psi}(\boldsymbol{\gamma}^t, \boldsymbol{\omega}^t) \triangleq \frac{1}{2}\begin{bmatrix}\boldsymbol{\gamma}^t \\ \boldsymbol{\omega}^t\end{bmatrix}^{\mathrm{T}}\begin{bmatrix}\boldsymbol{C}_T & \mathbf{0}_{3\times 3} \\ \mathbf{0}_{3\times 3} & \boldsymbol{C}_R\end{bmatrix}\begin{bmatrix}\boldsymbol{\gamma}^t \\ \boldsymbol{\omega}^t\end{bmatrix} \tag{19}$$

and where extension and shearing $\boldsymbol{\gamma}^t$, defined as

$$\boldsymbol{\gamma}^t = (\boldsymbol{R}_t^e)^{\mathrm{T}}(\partial_s \boldsymbol{\varphi} - \boldsymbol{t}_1), \tag{20}$$

and curvature $\boldsymbol{\omega}^t$ are the material strain measures, and

$$\boldsymbol{C}_T = \mathrm{diag}[EA, GA_2, GA_3], \tag{21}$$

$$\boldsymbol{C}_R = \mathrm{diag}[GJ, EI_2, EI_3]. \tag{22}$$

The constants E and G are interpreted as Young's modulus and the shear modulus, A is the cross-sectional area of the pipe, A_2 and A_3 are the effective shear areas, I is the unit polar moment of inertia of the cross-section plane, and J is the Saint Venant torsional modulus. Hence in material form

$$\boldsymbol{n}^t = \boldsymbol{C}_T \boldsymbol{\gamma}^t, \tag{23}$$

$$\boldsymbol{m}^t = \boldsymbol{C}_R \boldsymbol{\omega}^t, \tag{24}$$

and in spatial form

$$\boldsymbol{n}^e = \boldsymbol{R}_t^e \boldsymbol{n}^t = \boldsymbol{R}_t^e \boldsymbol{C}_T (\boldsymbol{R}_t^e)^{\mathrm{T}}[\partial_S \boldsymbol{\varphi} - \boldsymbol{t}_1^e], \tag{25}$$

$$\boldsymbol{m}^e = \boldsymbol{R}_t^e \boldsymbol{m}^t = \boldsymbol{R}_t^e \boldsymbol{C}_R (\boldsymbol{R}_t^e)^{\mathrm{T}} \boldsymbol{\omega}^e. \tag{26}$$

Taking the time derivative of (20) yields $\dot{\boldsymbol{\gamma}}^t$ to be

$$\dot{\boldsymbol{\gamma}}^t = -\boldsymbol{S}(\mathbf{w}^t)(\boldsymbol{R}_t^e)^{\mathrm{T}}(\partial_S \boldsymbol{\varphi}) + (\boldsymbol{R}_t^e)^{\mathrm{T}}(\partial_S \dot{\boldsymbol{\varphi}}) = (\boldsymbol{R}_t^e)^{\mathrm{T}}[\partial_S \dot{\boldsymbol{\varphi}} - \mathbf{w}^e \times (\partial_S \boldsymbol{\varphi})]. \tag{27}$$

2.5. Dynamics

The linear and angular momentum balance equations for a nonlinear elastic beam are derived in Simo (1985) as

$$m_P \ddot{\boldsymbol{\varphi}} = \partial_S \boldsymbol{n}^e + \tilde{\boldsymbol{n}}^e, \tag{28}$$

$$\boldsymbol{I}_\rho^e \dot{\mathbf{w}}^e + \mathbf{w}^e \times \boldsymbol{I}_\rho^e \mathbf{w}^e = \partial_S \boldsymbol{m}^e + (\partial_S \boldsymbol{\varphi}) \times \boldsymbol{n}^e + \tilde{\boldsymbol{m}}^e, \tag{29}$$

where m_P is the mass per unit length, $\tilde{\boldsymbol{n}}^e$ and $\tilde{\boldsymbol{m}}^e$ are the resultant external force and torque per unit length, and $\boldsymbol{I}_\rho^e(S,t)$ is the state dependent inertia tensor given by

$$\boldsymbol{I}_\rho^e = \boldsymbol{R}_t^e \boldsymbol{J}_\rho^t (\boldsymbol{R}_t^e)^{\mathrm{T}}, \quad \boldsymbol{J}_\rho^t = \mathrm{diag}[J_1, J_2, J_3] \geq 0, \tag{30}$$

where $\boldsymbol{J}_\rho^t$ is the constant inertia tensor for the cross-sections in the reference configuration.

In this paper we propose to adopt this model for pipes submerged in water by approximating $\tilde{\boldsymbol{n}}^e$ and $\tilde{\boldsymbol{m}}^e$ by

$$\tilde{\boldsymbol{n}}^e = -\boldsymbol{f}_g^e - \boldsymbol{f}_D^e - \boldsymbol{\sigma}^e, \tag{31}$$

$$\tilde{\boldsymbol{m}}^e = -\boldsymbol{D}_R \mathbf{w}^e, \tag{32}$$

where $\boldsymbol{f}_g^e$ is the restoring forces vector (gravitation and buoyancy), $\boldsymbol{f}_D^e$ the transversal hydrodynamic damping, $\boldsymbol{D}_R$ the constant damping matrix of rotation, $\boldsymbol{\sigma}^e$ the seabed interaction force. Hence, the equations of motion for a nonlinear elastic pipe submerged in water, given as a PDE in the spatial frame, is found by substituting (31)–(32) into (28)–(29).

2.5.1. Hydrostatic restoring terms

The pipe is assumed to be completely submerged in water such that the restoring forces per unit length are the sum of the gravitation and the buoyancy as defined by Archimedes. The restoring forces acts only in the vertical direction $\boldsymbol{e}_3$, and is given in $\boldsymbol{e}$ by

$$\boldsymbol{f}_g^e = (m_P - \rho_w A) g \boldsymbol{e}_3, \tag{33}$$

where ρ_w is the mass density of ambient water, A is the pipe cross-section area and g is the gravitational constant.

2.5.2. Hydrodynamic damping terms

The hydrodynamic forces on a submerged slender body are given by Morison's equation as the sum of added mass and drag (Morison et al., 1950). For applications involving low velocities such as e.g., risers, mooring lines and pipelay operations, the added mass term is small and can be neglected. An estimate for the remaining drag forces acting on a cylindrical shape in three dimensions are

$$\boldsymbol{f}_D^t = \frac{1}{2} d_o \rho_w \boldsymbol{D}_T \begin{bmatrix} |v_{r_1}^t| v_{r_1}^t \\ ((v_{r_2}^t)^2 + (v_{r_3}^t)^2)^{1/2} v_{r_2}^t \\ ((v_{r_2}^t)^2 + (v_{r_3}^t)^2)^{1/2} v_{r_3}^t \end{bmatrix}, \tag{34}$$

where d_o is the outer pipe diameter and

$$\boldsymbol{D}_T = \mathrm{diag}[D_1, D_2, D_3], \tag{35}$$

where $D_1, D_2, D_3 \geq 0$ are damping coefficients, which are constant if a constant Reynold's number is assumed. The vector $\boldsymbol{v}_r^t$ is the relative velocity of the pipe in the water,

$$\boldsymbol{v}_r^t = (\boldsymbol{R}_t^e)^{\mathrm{T}}(\dot{\boldsymbol{\varphi}}^e - \boldsymbol{v}_c^e), \tag{36}$$

where $\boldsymbol{v}_c^e = \boldsymbol{v}_c^e(\boldsymbol{\varphi}^{\mathrm{T}} \boldsymbol{e}_3, t)$ is the water current vector given in the spatial frame. Let the rotational damping in (29) be directly proportional to the angular velocity $\mathbf{w}$, where

$$\boldsymbol{D}_R = \mathrm{diag}[D_4, D_5, D_6], \tag{37}$$

where $D_4, D_5, D_6 \geq 0$ are the damping coefficients.

2.6. Seabed interaction

A seabed interaction force is commonly modeled by a spring and damper pair or simply a spring, since the spring effect will usually dominate the damping effect. In this paper the damping effect is neglected, and we propose that the seabed interaction force $\boldsymbol{\sigma}^e$ is modeled by a nonlinear spring, acting on the pipeline

section that is in contact with the seabed, given by

$$\boldsymbol{\sigma}^e = k_\sigma(\kappa)\boldsymbol{e}_3, \quad k_\sigma(\kappa) = \begin{cases} 0, & \kappa < 0 \\ \dfrac{\|\boldsymbol{f}_g^e\|_2}{(d_o/8 - d_o/40)} \dfrac{10\kappa^2}{d_o}, & 0 \le \kappa \le d_o/20 \\ \dfrac{\|\boldsymbol{f}_g^e\|_2}{(d_o/8 - d_o/40)}(\kappa - d_o/40), & \kappa > d_o/20, \end{cases} \tag{38}$$

where $\kappa = \boldsymbol{\varphi}^{\mathrm{T}}\boldsymbol{e}_3 + d_o/2$ denotes the vertical seabed penetration. The nonlinear spring $\boldsymbol{\sigma}^e \in \mathcal{C}^1$ is defined such that the pipe is at rest for seabed penetration equal to $1/8$ of the outer pipe diameter, $\kappa = d_o/8$. The spring becomes linear for $\kappa > d_o/20$ and the constants are chosen so that $\boldsymbol{\sigma}^e$ becomes continuously differentiable over $\mathbb{R}$.

2.7. Boundary conditions

Model (28)–(29) is clamped to the seabed at the lower end and fixed to a surface vessel at the upper end. These boundary conditions are presented in this section, mainly focusing on the surface vessel model.

2.7.1. Seabed

The lower end of the pipe is assumed to be fixed to the seabed, and the boundary condition for $S = 0$ is thus given by

$$\boldsymbol{\varphi}(0,t) = \boldsymbol{\varphi}_0 = 0, \quad \boldsymbol{R}_t^e(0,t) = \boldsymbol{R}_{t,0}^e = \boldsymbol{I}_{3\times 3}. \tag{39}$$

2.7.2. Vessel

In recent years there has been a significant drive to develop time-domain models for simulation and control system design based on data obtained from seakeeping programs such as VERES (Fathi, 2004) and WAMIT (2004). These programs use potential theory to compute the potential coefficients (added mass and potential damping) and the existing wave loads (Froude–Krylov and diffraction forces) for a given vessel design Fossen (2002) and Fossen and Smogeli (2004). In Perez and Fossen (2007), a potential theory formulation for a surface vessel suited for dynamic positioning and low speed maneuvering is developed, and this model is adopted as the boundary condition of the pipe at $S = L$ with some modifications.

Let $\boldsymbol{\eta} \in \mathbb{R}^3 \times \mathcal{S}^3$ be the generalized coordinate position vector using Euler angles given in the spatial frame $\boldsymbol{e}$ and $\boldsymbol{\nu} \in \mathbb{R}^6$ be the generalized velocity vector given in the body frame $\boldsymbol{b}$, both defined by Fossen (2002) as

$$\boldsymbol{\eta} = [x, y, z, \varphi, \theta, \psi]^{\mathrm{T}} \quad \text{and} \quad \boldsymbol{\nu} = [u, v, w, p, q, r]^{\mathrm{T}}. \tag{40}$$

For low-speed applications, we can approximate the equations of motion with a linear kinetic model,

$$\boldsymbol{M}\dot{\boldsymbol{\nu}} + \boldsymbol{C}_{RB}\boldsymbol{\nu} + \boldsymbol{C}_A\boldsymbol{\nu} + \boldsymbol{B}(\infty)\boldsymbol{\nu} + \boldsymbol{\mu} + \boldsymbol{G}\boldsymbol{\eta} = \boldsymbol{\tau} + \boldsymbol{\chi} + \upsilon, \tag{41}$$

while the kinematics use a nonlinear formulation

$$\dot{\boldsymbol{\eta}} = \boldsymbol{J}(\boldsymbol{\eta})\boldsymbol{\nu}, \quad \boldsymbol{J}(\boldsymbol{\eta}) = \begin{bmatrix} \boldsymbol{R}_b^e & \boldsymbol{0}_{3\times 3} \\ \boldsymbol{0}_{3\times 3} & \boldsymbol{t}_\Theta \end{bmatrix}, \tag{42}$$

where $\boldsymbol{T}_\Theta$ relates the body-fixed angular velocity to the Euler rate vector. Let

$$\boldsymbol{M} \triangleq \boldsymbol{M}_{RB} + \boldsymbol{M}_A, \tag{43}$$

where $\boldsymbol{M}_{RB}$ is the rigid body inertia matrix

$$\boldsymbol{M}_{RB} = \begin{bmatrix} m_V\boldsymbol{I}_{3\times 3} & \boldsymbol{0}_{3\times 3} \\ \boldsymbol{0}_{3\times 3} & \boldsymbol{I}_V^b \end{bmatrix}, \tag{44}$$

where m_V is the total vessel mass, and $\boldsymbol{I}_V^b \in \mathbb{R}^{3\times 3}$ is the body inertia tensor. Matrix $\boldsymbol{M}_A = \boldsymbol{A}(\infty)$ and $\boldsymbol{B}(\infty)$ are the constant infinite frequency added mass and potential damping matrices. Notice that $\boldsymbol{B}(\infty) = 0$ for zero-speed applications. As the frame used is not inertial, the Coriolis and centripetal terms for the rigid body $\boldsymbol{C}_{RB}$ and the added mass $\boldsymbol{C}_A$ are accounted for, and appears as

$$\boldsymbol{C}_{RB} \triangleq \boldsymbol{M}_{RB}U\boldsymbol{L} \quad \text{and} \quad \boldsymbol{C}_A \triangleq \boldsymbol{M}_A U\boldsymbol{L}, \tag{45}$$

where $U = \|\boldsymbol{\nu}^e\|$, and

$$\boldsymbol{L} \triangleq \begin{bmatrix} 0 & \cdots & 0 & 0 \\ 0 & \cdots & 0 & 1 \\ 0 & \cdots & -1 & 0 \\ \vdots & \ddots & \vdots & \vdots \\ 0 & \cdots & 0 & 0 \end{bmatrix} \in \mathbb{R}^{6\times 6}. \tag{46}$$

The matrix $\boldsymbol{G}$ is the restoring matrix. The external forces acting on the pipelay vessel are the control forces $\boldsymbol{\tau}$, typically from thrusters controlled by a DP system, the forces and moments from the pipe string extending from the vessel $\boldsymbol{\chi}$, and the environmental loads υ. For the remainder of this paper $\upsilon = 0$ is assumed.

For t the term $\boldsymbol{\mu}$ is a convolution term representing the fluid memory effects and given for low-speed, i.e. $U = 0$, as

$$\boldsymbol{\mu} \triangleq \int_0^t \boldsymbol{K}(t-\xi)\boldsymbol{\nu}(\xi)\, d\xi, \tag{47}$$

where $\boldsymbol{K}(t)$ is a matrix of retardation functions (Ogilvie, 1964)

$$\boldsymbol{K}(t) = \int_0^\infty \boldsymbol{B}(\omega)\cos(\omega t)\, d\omega. \tag{48}$$

We can approximate

$$\boldsymbol{\mu}(t) \approx \boldsymbol{D}_p\boldsymbol{\nu}, \tag{49}$$

where $\boldsymbol{D}_p$ is a frequency-independent constant matrix approximating $\boldsymbol{\mu}$ at low frequencies. The resulting linear state-space model becomes

$$\boldsymbol{M}\dot{\boldsymbol{\nu}} + \boldsymbol{C}_{RB}\boldsymbol{\nu} + \boldsymbol{C}_A\boldsymbol{\nu} + \boldsymbol{\mu} + \boldsymbol{G}\boldsymbol{\eta} = \boldsymbol{\tau} + \boldsymbol{\chi} + \upsilon. \tag{50}$$

In hydrodynamics it is common to assume linear superposition (Faltinsen, 1990), hence nonlinear Coriolis and damping terms can be added directly in the time-domain model (50) according to

$$\boldsymbol{M}\dot{\boldsymbol{\nu}} + \boldsymbol{C}(\boldsymbol{\nu})\boldsymbol{\nu} + \boldsymbol{D}(\boldsymbol{\nu})\boldsymbol{\nu} + \boldsymbol{g}(\boldsymbol{\varphi}, \boldsymbol{R}_b^e) = \boldsymbol{\tau} + \boldsymbol{\chi} + \upsilon, \tag{51}$$

with relaxations

$$\boldsymbol{G}\boldsymbol{\eta} \longleftrightarrow \boldsymbol{g}(\boldsymbol{\varphi}, \boldsymbol{R}_b^e), \tag{52}$$

$$\boldsymbol{C}_{RB} \longleftrightarrow \boldsymbol{C}_{RB}(\boldsymbol{\nu}), \tag{53}$$

$$\boldsymbol{C}_A \longleftrightarrow \boldsymbol{C}_A(\boldsymbol{\nu}), \tag{54}$$

and

$$\boldsymbol{C}(\boldsymbol{\nu}) \triangleq \boldsymbol{C}_{RB}(\boldsymbol{\nu}) + \boldsymbol{C}_A(\boldsymbol{\nu}), \tag{55}$$

$$\boldsymbol{D}(\boldsymbol{\nu}) \triangleq \boldsymbol{D}_p + \boldsymbol{D}_v(\boldsymbol{\nu}), \tag{56}$$

where $\boldsymbol{D}_v(\boldsymbol{\nu})$ is quadratic viscous damping due to cross-flow drag and surge resistance.

The following properties of (51) holds for the assumption that $\dot{\boldsymbol{M}} = \boldsymbol{0}$:

(P1) $\boldsymbol{M} = \boldsymbol{M}^{\mathrm{T}} > 0$,
(P2) $\boldsymbol{s}^{\mathrm{T}}[\dot{\boldsymbol{M}} - 2\boldsymbol{C}(\boldsymbol{\nu})]\boldsymbol{s} = 0, \forall \boldsymbol{s} \in \mathbb{R}^6$,
(P3) $\boldsymbol{D}(\boldsymbol{\nu}) > 0, \forall \boldsymbol{\nu} \in \mathbb{R}^6$.

A metacentric stable surface vessel has restoring forces and moments in heave (z), roll (ϕ) and pitch (θ) that will resist inclinations away from the steady-state equilibrium. The restoring forces and moments will depend on the vessel's metacentric height, the location of the center of gravity, the center of buoyancy, and the shape and size of the water plane, denoted

by A_{wp}. For every vessel and load a transversal metacentric height $\overline{GM}_T \in \mathbb{R}$ and a longitudinal metacentric height $\overline{GM}_L \in \mathbb{R}$ can be computed (Fossen, 2002).

The equilibrium in heave is obtained when the gravity and buoyancy forces balance. A force $\boldsymbol{g}_l^e \in \mathbb{R}^3$ is generated to restore this balance if the heave position $\boldsymbol{\varphi}^{\mathrm{T}}(L,t)\boldsymbol{e}_3$ changed due to external forces, or the heave equilibrium z_{eq} changes due to, e.g., waves. This force is modeled in the $\boldsymbol{e}$ frame as

$$\boldsymbol{g}_l^e = -A_{wp}\rho_w g(\boldsymbol{\varphi}^{\mathrm{T}}(L,t)\boldsymbol{e}_3 - z_{eq})\boldsymbol{e}_3, \tag{57}$$

where the A_{wp} is assumed to be constant for small changes in heave.

From geometric considerations, the moment arms in roll and pitch can be found to be

$$\boldsymbol{r}_r^b = \begin{bmatrix} -\overline{GM}_L \sin\theta \\ \overline{GM}_T \sin\varphi \\ 0 \end{bmatrix}. \tag{58}$$

The dependence of Euler angles are removed from (58) by observing that

$$\sin(\theta) = -(\boldsymbol{R}_b^e \boldsymbol{e}_1)^{\mathrm{T}}\boldsymbol{e}_3, \tag{59}$$

$$\sin(\phi) \approx \cos(\theta)\sin(\phi) = (\boldsymbol{R}_b^e \boldsymbol{e}_2)^{\mathrm{T}}\boldsymbol{e}_3, \tag{60}$$

where the applied approximation $\cos(\theta) = 1$ is generally true for small pitch angles, hence (58) is approximated by without Euler angles as

$$\tilde{\boldsymbol{r}}_r^b \triangleq \begin{bmatrix} \overline{GM}_L(\boldsymbol{R}_b^e \boldsymbol{e}_1)^{\mathrm{T}}\boldsymbol{e}_3 \\ \overline{GM}_T(\boldsymbol{R}_b^e \boldsymbol{e}_2)^{\mathrm{T}}\boldsymbol{e}_3 \\ 0 \end{bmatrix} \approx \boldsymbol{r}_r^b \tag{61}$$

such that the restoring moment term becomes

$$\boldsymbol{g}_r^e = \tilde{\boldsymbol{r}}_r^e \times \boldsymbol{f}_r^e = (\boldsymbol{R}_b^e \tilde{\boldsymbol{r}}_r^b) \times (m_V g \boldsymbol{e}_3). \tag{62}$$

It is assumed that there is no moment due to heave. Consequently, the nonlinear restoring forces term of (51) is given in the body frame $\boldsymbol{b}$ as

$$\boldsymbol{g}^b(\boldsymbol{\varphi}(L,t), \boldsymbol{R}_b^e(t)) = \begin{bmatrix} (\boldsymbol{R}_b^e)^{\mathrm{T}}\boldsymbol{g}_t^e \\ (\boldsymbol{R}_b^e)^{\mathrm{T}}\boldsymbol{g}_r^e \end{bmatrix}. \tag{63}$$

For the remainder of this paper, let the pipe be fixed to the center of gravity of the vessel such that

$$\boldsymbol{v} = \begin{bmatrix} (\boldsymbol{R}_b^e)^{\mathrm{T}}\dot{\boldsymbol{\varphi}}(L,t) \\ (\boldsymbol{R}_b^e)^{\mathrm{T}}\mathbf{w}^e(L,t) \end{bmatrix} \quad \text{and} \quad \dot{\boldsymbol{v}} = \begin{bmatrix} (\boldsymbol{R}_b^e)^{\mathrm{T}}\ddot{\boldsymbol{\varphi}}(L,t) \\ (\boldsymbol{R}_b^e)^{\mathrm{T}}\dot{\mathbf{w}}^e(L,t) \end{bmatrix}. \tag{64}$$

Forces and moments acting between the pipe and the vessel are considered as internal forces in the total system, and by Newton's third law the following relationship holds:

$$\begin{bmatrix} \overline{\boldsymbol{n}}^e(L,t) \\ \overline{\boldsymbol{m}}^e(L,t) \end{bmatrix} = -\begin{bmatrix} \boldsymbol{R}_b^e & \mathbf{0}_{3\times3} \\ \mathbf{0}_{3\times3} & \boldsymbol{R}_b^e \end{bmatrix} \boldsymbol{\chi}. \tag{65}$$

3. Passivity

The passivity properties of the developed model, with and without boundary conditions, are considered in this section. Passivity provides a useful tool for the analysis of nonlinear systems which relates nicely to Lyapunov and $\mathcal{L}_2$ stability (Khalil, 2002). The main passivity theorem states that the negative feedback connection of two passive systems is passive. By proving passivity of the pipelay system and choosing a passive controller, the feedback connection is thus known to be stable, which is necessary for control applications.

Theorem 3.1. *System* (28)–(29) *is input–output passive, where the input* $\overline{\boldsymbol{\tau}}$ *and output* $\overline{\boldsymbol{v}}$ *are taken as*

$$\overline{\boldsymbol{\tau}} \triangleq [\overline{\boldsymbol{n}}^e(0,t), \overline{\boldsymbol{m}}^e(0,t), \overline{\boldsymbol{n}}^e(L,t), \overline{\boldsymbol{m}}^e(L,t)]^{\mathrm{T}} \in \mathbb{R}^{12}, \tag{66}$$

$$\overline{\boldsymbol{v}} \triangleq [-\dot{\boldsymbol{\varphi}}(0,t), -\mathbf{w}^e(0,t), \dot{\boldsymbol{\varphi}}(L,t)\mathbf{w}^e(L,t)]^{\mathrm{T}} \in \mathbb{R}^{12} \tag{67}$$

and assuming that $|v_{c,i}^e| \le |\dot{\phi}_i|$, *for* $i = 1, \ldots, 3$ (36).

Proof. The total system energy $\mathcal{E}_P$ of (28)–(29), is given by

$$\mathcal{E}_P = \mathcal{T}_P + \mathcal{U}_P, \tag{68}$$

where this pipe energy function is the sum of kinetic energy $\mathcal{T}_P$ and potential energy $\mathcal{U}_P$ (Simo and Vu-Quoc, 1986),

$$\mathcal{T}_P = \frac{1}{2}\int_0^L m_p \|\dot{\boldsymbol{\varphi}}\|_2^2 + \langle \mathbf{w}^e, \boldsymbol{I}_\rho^e \mathbf{w}^e \rangle \, dS, \tag{69}$$

$$\mathcal{U}_P = \int_0^L \boldsymbol{\Psi}(\boldsymbol{\gamma}^t, \boldsymbol{\omega}^t)\, dS + \int_0^L \left(\langle \boldsymbol{f}_g^e, \boldsymbol{\varphi} \rangle + \int_0^\kappa k_\sigma(\xi) d\xi \right) dS. \tag{70}$$

Differentiating (68) with respect to time, the kinetic energy term yields

$$\dot{\mathcal{T}}_P = \int_0^L \langle \dot{\boldsymbol{\varphi}}, m_p \ddot{\boldsymbol{\varphi}} \rangle + \langle \mathbf{w}^e, \boldsymbol{I}_\rho^e \dot{\mathbf{w}}^e \rangle \, dS, \tag{71}$$

which by substituting by (28)–(29) can be rewritten as

$$\begin{aligned} \dot{\mathcal{T}}_P = \int_0^L \langle \dot{\boldsymbol{\varphi}}, [\partial_S \boldsymbol{n}^e - \boldsymbol{f}_g^e - \boldsymbol{f}_D^e - \boldsymbol{\sigma}^e] \rangle \, dS + \int_0^L \langle \mathbf{w}^e, [(\boldsymbol{I}_\rho^e \mathbf{w}^e) \\ \times \mathbf{w}^e + \partial_S \boldsymbol{m}^e + (\partial_S \boldsymbol{\varphi}) \times \boldsymbol{n}^e - \boldsymbol{D}_R \mathbf{w}^e] \rangle \, dS. \end{aligned} \tag{72}$$

The potential energy rate of change yields by differentiation

$$\dot{\mathcal{U}}_P = \int_0^L \langle \boldsymbol{n}^t, \partial_t \boldsymbol{\gamma}^t \rangle + \langle \boldsymbol{m}^t, \partial_t \boldsymbol{\omega}^t \rangle \, dS + \int_0^L \langle \boldsymbol{f}_g^e, \dot{\boldsymbol{\varphi}} \rangle + \langle \boldsymbol{\sigma}^e, \dot{\boldsymbol{\varphi}} \rangle \, dS \tag{73}$$

which by substitution of (27) for $\partial_t \boldsymbol{\gamma}^t$ and (17) for $\partial_t \boldsymbol{\omega}^t$, is rewritten as

$$\begin{aligned} \dot{\mathcal{U}}_P = \int_0^L \langle \boldsymbol{n}^e, [\partial_S \dot{\boldsymbol{\varphi}} - (\mathbf{w}^e \times (\partial_S \boldsymbol{\varphi}))] \rangle \, dS + \int_0^L \langle \boldsymbol{m}^t, [\partial_S \mathbf{w}^t + (\boldsymbol{\omega}^t \\ \times \mathbf{w}^t)] \rangle \, dS + \int_0^L \langle \boldsymbol{f}_g^e, \dot{\boldsymbol{\varphi}} \rangle + \langle \boldsymbol{\sigma}^e, \dot{\boldsymbol{\varphi}} \rangle \, dS. \end{aligned} \tag{74}$$

Since

$$\partial_S \mathbf{w}^e = \partial_S(\boldsymbol{R}_t^e \mathbf{w}^t) = \boldsymbol{R}_t^e \boldsymbol{S}(\boldsymbol{\omega}^t)\mathbf{w}^t + \boldsymbol{R}_t^e \partial_S \mathbf{w}^t = \boldsymbol{R}_t^e [\partial_S \mathbf{w}^t + (\boldsymbol{\omega}^t \times \mathbf{w}^t)] \tag{75}$$

and the fact that $\langle \boldsymbol{m}^t, (\boldsymbol{R}_t^e)^{\mathrm{T}} \partial_S \mathbf{w}^e \rangle = \langle \boldsymbol{m}^e, \partial_S \mathbf{w}^e \rangle$, the second term in (74) is simplified, and by partial integration, Eq. (74) is finally rewritten as

$$\begin{aligned} \dot{\mathcal{U}}_P = \langle \overline{\boldsymbol{n}}^e, \dot{\boldsymbol{\varphi}} \rangle|_0^L + \langle \overline{\boldsymbol{m}}^e, \mathbf{w}^e \rangle|_0^L - \int_0^L \langle \partial_S \boldsymbol{n}^e, \dot{\boldsymbol{\varphi}} \rangle + \langle \partial_S \boldsymbol{m}^e, \mathbf{w}^e \rangle \\ + \langle \mathbf{w}^e, (\partial_S \boldsymbol{\varphi}) \times \boldsymbol{n}^e \rangle \, dS \\ + \int_0^L \langle \boldsymbol{f}_g^e, \dot{\boldsymbol{\varphi}} \rangle + \langle \boldsymbol{\sigma}^e, \dot{\boldsymbol{\varphi}} \rangle \, dS. \end{aligned} \tag{76}$$

Hence, the change of energy of the pipe string $\dot{\mathcal{E}}_P$ can then be found by summing (72) and (76) as

$$\dot{\mathcal{E}}_P = \langle \overline{\boldsymbol{n}}^e, \dot{\boldsymbol{\varphi}} \rangle|_0^L + \langle \overline{\boldsymbol{m}}^e, \mathbf{w}^e \rangle|_0^L - \int_0^L \langle \dot{\boldsymbol{\varphi}}, \boldsymbol{f}_D^e \rangle \, dS - \int_0^L \langle \mathbf{w}^e, \boldsymbol{D}_R \mathbf{w}^e \rangle \, dS, \tag{77}$$

where the energy is seen to depend on the boundary conditions and the transversal and rotational damping. Investigating the integral term for the rotational damping it is readily seen that

$$\int_0^L \langle \mathbf{w}^e, \boldsymbol{D}_R \mathbf{w}^e \rangle \, dS = \int_0^L \sum_{i=1}^3 D_{i+3} (\mathbf{w}_i^e)^2 \Big) \, dS \ge 0, \quad \forall \mathbf{w}^e \tag{78}$$

such that this term will always dissipate energy. The restoring term is rewritten into

$$\int_0^L \langle \dot{\boldsymbol{\varphi}}, \boldsymbol{f}_D^e \rangle \, dS = \frac{1}{2} d\rho_w \int_0^L \langle \dot{\boldsymbol{\varphi}}, \boldsymbol{\Pi}(\dot{\boldsymbol{\varphi}} - \boldsymbol{v}_c^e) \rangle \, dS \geq 0, \quad \forall |v_{c,i}^e| \leq |\dot{\phi}_i|, \tag{79}$$

where

$$\boldsymbol{\Pi} = \boldsymbol{R}_t^e \boldsymbol{D}_T \boldsymbol{\Gamma} (\boldsymbol{R}_t^e)^{\mathrm{T}} \geq 0, \tag{80}$$

$$\boldsymbol{\Gamma} = \mathrm{diag}[|v_{r_1}^t|, ((v_{r_2}^t)^2 + (v_{r_3}^t)^2)^{1/2}, ((v_{r_2}^t)^2 + (v_{r_3}^t)^2)^{1/2}] \geq 0. \tag{81}$$

Hence, from (77) and the assumption $|v_{c,i}^e| \leq |\dot{\phi}_i|$, it follows that

$$\dot{\mathcal{E}}_P \leq \langle \overline{\boldsymbol{n}}^e, \dot{\boldsymbol{\varphi}} \rangle |_0^L + \langle \overline{\boldsymbol{m}}^e, \mathbf{w}^e \rangle |_0^L = \overline{\boldsymbol{\tau}}^{\mathrm{T}} \overline{\boldsymbol{v}}. \qquad \square \tag{82}$$

This theorem can be extended to also include the boundary conditions.

Theorem 3.2. *System* (28)–(29) *with boundary condition* (39) *for* $S = 0$ *and* (65) *for* $S = L$ *is input–output passive, with input* $\boldsymbol{\tau}$ *and output* $\boldsymbol{v}$ (40)*, and assuming that* $|v_{c,i}^e| \leq |\dot{\phi}_i|$*, for* $i = 1, \ldots, 3$.

Proof. The total energy $\mathcal{E}$ of the pipelay system is given by the sum of the total energy of the pipe $\mathcal{E}_P$ and the surface vessel $\mathcal{E}_V$,

$$\mathcal{E} = \mathcal{E}_P + \mathcal{E}_V \geq 0, \tag{83}$$

$$\mathcal{E}_V = \mathcal{T}_V + \mathcal{U}_V. \tag{84}$$

The vessel energy function is the sum of kinetic $\mathcal{T}_V$ and potential energy $\mathcal{U}_V$,

$$\mathcal{T}_V = \tfrac{1}{2} \boldsymbol{v}^{\mathrm{T}} \boldsymbol{M} \boldsymbol{v}, \tag{85}$$

$$\begin{aligned} \mathcal{U}_V = {} & \tfrac{1}{2} A_{wp} \rho_w g (\boldsymbol{\varphi}^{\mathrm{T}}(L,t) \boldsymbol{e}_3 + h_{ref})^2 + \tfrac{1}{2} m_V g \{ \overline{GM}_L [(\boldsymbol{R}_b^e \boldsymbol{e}_1)^{\mathrm{T}} \boldsymbol{e}_3]^2 \\ & + \overline{GM}_T [(\boldsymbol{R}_b^e \boldsymbol{e}_2)^{\mathrm{T}} \boldsymbol{e}_3]^2 \}, \end{aligned} \tag{86}$$

where $\mathcal{U}_V$ is the sum of the potential functions derived from (57) and (63). By differentiating (85) and (86) with respect to time, and substituting in (51) and finally applying property **P2**, the change of energy for the vessel is found to be

$$\dot{\mathcal{T}}_V = \boldsymbol{v}^{\mathrm{T}} (\boldsymbol{\tau} + \boldsymbol{\chi}) - \boldsymbol{v}^{\mathrm{T}} \boldsymbol{D} \boldsymbol{v} - \boldsymbol{v}^{\mathrm{T}} \boldsymbol{g}, \tag{87}$$

$$\dot{\mathcal{U}}_V = \boldsymbol{v}^{\mathrm{T}} \boldsymbol{g}, \tag{88}$$

which is summed to express $\dot{\mathcal{E}}_V$ by

$$\dot{\mathcal{E}}_V = \boldsymbol{v}^{\mathrm{T}} (\boldsymbol{\tau} + \boldsymbol{\chi}) - \boldsymbol{v}^{\mathrm{T}} \boldsymbol{D} \boldsymbol{v}. \tag{89}$$

Applying property **P3** to (89) yields $\dot{\mathcal{E}}_V \leq \boldsymbol{v}^{\mathrm{T}} (\boldsymbol{\tau} + \boldsymbol{\chi})$ showing that the vessel is itself input–output passive with input $(\boldsymbol{\tau} + \boldsymbol{\chi})$ and output $\boldsymbol{v}$. Hence, the derivative of the energy (83) can be found by summing (77) and (89),

$$\begin{aligned} \dot{\mathcal{E}} = {} & \langle \overline{\boldsymbol{n}}^e, \dot{\boldsymbol{\varphi}} \rangle |_0^L + \langle \overline{\boldsymbol{m}}^e, \mathbf{w}^e \rangle |_0^L - \int_0^L \langle \dot{\boldsymbol{\varphi}}, \boldsymbol{f}_D^e \rangle \, dS \\ & - \int_0^L \langle \mathbf{w}^e, \boldsymbol{D}_R \mathbf{w}^e \rangle \, dS + \boldsymbol{v}^{\mathrm{T}} (\boldsymbol{\tau} + \boldsymbol{\chi}) - \boldsymbol{v}^{\mathrm{T}} \boldsymbol{D} \boldsymbol{v}, \end{aligned} \tag{90}$$

where the lower boundary condition $S = 0$, known from (39), implies

$$\langle \overline{\boldsymbol{n}}^e, \dot{\boldsymbol{\varphi}} \rangle |_0 = \langle \overline{\boldsymbol{m}}^e, \mathbf{w}^e \rangle |_0 = 0 \tag{91}$$

and the upper boundary condition is given by (65) where the pipe is connected to the vessel in the center of gravity, as defined in (64), such that the total rate of change of energy of the pipe and vessel system reduces to

$$\dot{\mathcal{E}} = - \int_0^L \langle \dot{\boldsymbol{\varphi}}, \boldsymbol{f}_D^e \rangle \, dS - \int_0^L \langle \mathbf{w}^e, \boldsymbol{D}_R \mathbf{w}^e \rangle \, dS - \boldsymbol{v}^{\mathrm{T}} \boldsymbol{D} \boldsymbol{v} + \boldsymbol{v}^{\mathrm{T}} \boldsymbol{\tau}, \tag{92}$$

which implies that $\dot{\mathcal{E}} \leq \boldsymbol{v}^{\mathrm{T}} \boldsymbol{\tau}$, and the system is input–output passive. $\square$

Corollary 3.3. *Finally, it can be concluded the combined system of pipeline and vessel is stable since* $\mathcal{E} \geq 0$, $\|\mathcal{E}\| \to \infty$ *due to unbounded system states, and* $\dot{\mathcal{E}} \leq 0$ *which implies that*

$$\mathcal{E}(t) - \mathcal{E}(0) \leq 0. \tag{93}$$

If a *passive* controller $\boldsymbol{\tau}$ is applied, this analysis shows that the complete system is input–output passive and stable.

4. Model validation

A validation of the proposed pipe model is performed to evaluate how accurate the model approximates the physical system. Since a physical system is not available for this validation, our model must be validated against other models, that are validated against real systems. The *natural catenary equation* is used for static validation, and the FEM code *RIFLEX* is used for both static and dynamic validation. The catenary equation is the classic nonlinear solution of the static deflection curve for a string loaded by its own weight, and is well known from cable mechanics (Irvine, 1981), while RIFLEX is a recognized FEM program for static and dynamic analyses of slender marine structures developed by MARINTEK and SINTEF in cooperation with the Norwegian University of Science and Technology (NTNU) as a joint industry project (Fylling et al., 2008).

The pipe model (28)–(29) is a continuous operator problem, that must be converted into a discrete problem to approximate the solution. The model validation is performed in two main steps:

1. *FEM model implementation*—A FEM model suitable for simulation is derived from the PDE (28)–(29) by application of a numerical finite element method.
2. *Numerical simulation*—A simulation scenario is defined for a pipeline, including corresponding material properties and pipelay parameters. The simulation data obtained from the FEM model, the natural catenary equation, and RIFLEX are then compared.

4.1. Numerical implementation

A finite element method is applied on (28)–(29) for the numerical simulations, following the same procedure as in Simo and Vu-Quoc (1988). A Galerkin weak form of the initial boundary problem (28)–(29) with boundary conditions (39) and (65), is developed by taking the inner product with admissible test functions $\boldsymbol{u}, \boldsymbol{\vartheta}$. Let the space of test functions $\mathcal{V}$ be defined as

$$\mathcal{V} = \{ (\boldsymbol{u}, \boldsymbol{\vartheta}) | S \in [0, L] \to \mathbb{R}^3 \times \mathbb{R}^3 | (\boldsymbol{u}, \boldsymbol{\vartheta})|_{S=0} = (\mathbf{0}, \mathbf{0}) \}. \tag{94}$$

Admissible variations associated with any pipe configuration $(\boldsymbol{\varphi}, \boldsymbol{R}_t^e) \in \mathcal{C}$ span the tangent space $T_{(\boldsymbol{\varphi}, \boldsymbol{R}_t^e)} \mathcal{C}$ given by

$$T_{(\boldsymbol{\varphi}, \boldsymbol{R}_t^e)} \mathcal{C} \triangleq \{ (\boldsymbol{u}, \boldsymbol{S}(\boldsymbol{\vartheta}) \boldsymbol{R}_t^e) | (\boldsymbol{u}, \boldsymbol{\vartheta}) \in \mathcal{V} \}. \tag{95}$$

Hence, the weak formulation is found to be

$$\begin{aligned} G_{\mathrm{dyn}}(\boldsymbol{\varphi}, \boldsymbol{R}_t^e; \boldsymbol{u}, \boldsymbol{\vartheta}) \triangleq {} & \int_0^L \langle m_P \ddot{\boldsymbol{\varphi}}, \boldsymbol{u} \rangle + \langle [\boldsymbol{I}_\rho \dot{\mathbf{w}}^e + \mathbf{w}^e \times (\boldsymbol{I}_\rho \mathbf{w}^e)], \boldsymbol{\vartheta} \rangle \, dS \\ & + \int_0^L \langle \boldsymbol{f}_D^e, \boldsymbol{u} \rangle + \langle \boldsymbol{D}_R \mathbf{w}^e, \boldsymbol{\vartheta} \rangle \, dS + G_{\mathrm{stat}}(\boldsymbol{\Phi}, \boldsymbol{R}_t^e; \boldsymbol{u}, \boldsymbol{\vartheta}) \\ & + \langle [\boldsymbol{M} \dot{\boldsymbol{v}} + \boldsymbol{C}(\boldsymbol{v}) \boldsymbol{v} + \boldsymbol{D}(\boldsymbol{v}) \boldsymbol{v}], (\boldsymbol{u}^{\mathrm{T}}, \boldsymbol{\vartheta}^{\mathrm{T}})^{\mathrm{T}} \rangle |_{S=L} = 0, \end{aligned} \tag{96}$$

for all test functions $(\boldsymbol{u},\boldsymbol{\vartheta})\in\mathcal{V}$, where the static part G_{stat} is given by

$$G_{\text{stat}}(\boldsymbol{\varphi},\boldsymbol{R}_t^e;\boldsymbol{u},\boldsymbol{\vartheta}) \triangleq \int_0^L \left\langle \boldsymbol{n}^e, \left[\frac{d\boldsymbol{u}}{dS}+\boldsymbol{S}(\partial_S\boldsymbol{\varphi})\boldsymbol{\vartheta}\right]\right\rangle + \left\langle \boldsymbol{m}^e, \frac{d\boldsymbol{\vartheta}}{dS}\right\rangle dS + \int_0^L \langle [\boldsymbol{f}_g^e+\boldsymbol{\sigma}^e], \boldsymbol{u}\rangle\, dS + \langle \boldsymbol{g}(\boldsymbol{\varphi},\boldsymbol{R}_b^e), (\boldsymbol{u}^{\mathrm{T}},\boldsymbol{\vartheta}^{\mathrm{T}})^{\mathrm{T}}\rangle|_{S=L}. \tag{97}$$

Now, let the rotation matrix $\boldsymbol{R}_t^e$ be parameterized in Euler angles $\boldsymbol{\Theta}=(\phi,\theta,\psi)^{\mathrm{T}}\to\boldsymbol{R}_t^e(\boldsymbol{\Theta})$ by the *zxy*-convention, which is locally diffeomorphic to $SO(3)$. Hence, $\boldsymbol{R}_t^e$ is given by

$$\boldsymbol{R}_t^e(\boldsymbol{\Theta})=\boldsymbol{R}_{\boldsymbol{e}_2}(\theta)\boldsymbol{R}_{\boldsymbol{e}_1}(\phi)\boldsymbol{R}_{\boldsymbol{e}_3}(\psi), \tag{98}$$

where the elementary rotations about the $\boldsymbol{e}_1$, $\boldsymbol{e}_2$ and $\boldsymbol{e}_3$ axes are given by

$$\boldsymbol{R}_{\boldsymbol{e}_1}(\phi)=\begin{bmatrix}1&0&0\\0&\mathrm{c}\phi&-\mathrm{s}\phi\\0&\mathrm{s}\phi&\mathrm{c}\phi\end{bmatrix},\quad \boldsymbol{R}_{\boldsymbol{e}_2}(\theta)=\begin{bmatrix}\mathrm{c}\theta&0&\mathrm{s}\theta\\0&1&0\\-\mathrm{s}\theta&0&\mathrm{c}\theta\end{bmatrix},$$
$$\boldsymbol{R}_{\boldsymbol{e}_3}(\psi)=\begin{bmatrix}\mathrm{c}\psi&-\mathrm{s}\psi&0\\\mathrm{s}\psi&\mathrm{c}\psi&0\\0&0&1\end{bmatrix}, \tag{99}$$

where s· and c· denotes sin(·) and cos(·). Adopting the *zxy*-convention instead of the more common *xyz*-convention moves the singularity inherent to Euler angles from pitch to roll, which is more suitable for the presented model. This choice of parametrization yields the transformations

$$\mathbf{w}^e=\boldsymbol{\Pi}_e\dot{\boldsymbol{\Theta}},\quad \dot{\mathbf{w}}^e=\boldsymbol{\Pi}_e\ddot{\boldsymbol{\Theta}}+\dot{\boldsymbol{\Pi}}_e\dot{\boldsymbol{\Theta}},$$
$$\partial_S\boldsymbol{\omega}^e=\boldsymbol{\Pi}_e(\partial_S\boldsymbol{\Theta}),\quad \boldsymbol{\Theta}=(\phi,\theta,\psi)^{\mathrm{T}}, \tag{100}$$

where

$$\boldsymbol{\Pi}_e=\begin{bmatrix}\mathrm{c}\theta&0&\mathrm{c}\phi\mathrm{s}\theta\\0&1&-\mathrm{s}\varphi\\-\mathrm{s}\theta&0&\mathrm{c}\phi\mathrm{c}\theta\end{bmatrix}. \tag{101}$$

Following the parametrization in Euler angles, the configuration space $\mathcal{C}$ can be reformulated as

$$\tilde{\mathcal{C}}\triangleq\{(\boldsymbol{\varphi},\boldsymbol{\Theta})|S\in[0,L]\to\mathbb{R}^3\times\mathbb{R}^3|\langle\partial_S\boldsymbol{\varphi}(S),\boldsymbol{R}_t^e(\boldsymbol{\Theta})\rangle\boldsymbol{e}_1>0\}, \tag{102}$$

with test functions

$$\tilde{\mathcal{V}}\triangleq\{(\boldsymbol{u},\tilde{\boldsymbol{\vartheta}})|S\in[0,L]\to\mathbb{R}^3\times\mathbb{R}^3|(\boldsymbol{u},\tilde{\boldsymbol{\vartheta}})|_{S=0}=(\boldsymbol{0},\boldsymbol{0})\} \tag{103}$$

and the new tangent space becomes

$$T_{(\boldsymbol{\varphi},\boldsymbol{\Theta})}\tilde{\mathcal{C}}\triangleq\{(\boldsymbol{u},\tilde{\boldsymbol{\vartheta}})|(\boldsymbol{u},\tilde{\boldsymbol{\vartheta}})\in\tilde{\mathcal{V}}\}. \tag{104}$$

The weak formulation (96) for the configuration space (102) is semi-discretized for N nodes with uniform sub interval $\bigcup_{i=1}^{N-1}[S_i,S_{i+1}]=[0,L]$ using linear shape functions $N_h^i(S)$ such that

$$\boldsymbol{\varphi}\approx\boldsymbol{\varphi}_h=\sum_{i=1}^N\boldsymbol{\varphi}_i(t)N_h^i(S),\quad \boldsymbol{\Theta}\approx\boldsymbol{\Theta}_h=\sum_{i=1}^N\boldsymbol{\Theta}_i(t)N_h^i(S),$$
$$\boldsymbol{u}_h=\sum_{i=1}^N\boldsymbol{u}_iN_h^i(S),\quad \tilde{\boldsymbol{\vartheta}}_h=\sum_{i=1}^N\tilde{\boldsymbol{\vartheta}}_iN_h^i(S) \tag{105}$$

and the integrals in the weak formulation $G_{\text{dyn}}(\boldsymbol{\varphi},\boldsymbol{R}_t^e(\boldsymbol{\Theta});\boldsymbol{u},\tilde{\boldsymbol{\vartheta}})$ (96) are approximated using two point Gaussian quadrature for each interval $[S_i,S_{i+1}]\subset[0,L]$, except for the stiffness integral

$$\int_0^L\left\langle\boldsymbol{n}^e,\left[\frac{d\boldsymbol{u}}{dS}+\boldsymbol{S}(\partial_S\boldsymbol{\varphi})\tilde{\boldsymbol{\vartheta}}\right]\right\rangle+\left\langle\boldsymbol{m}^e,\frac{d\tilde{\boldsymbol{\vartheta}}}{dS}\right\rangle dS, \tag{106}$$

which is approximated by a reduced one point Gaussian quadrature to avoid shear locking (Simo and Vu-Quoc, 1986). The semi-discretized problem is finally obtained on the form

$$\overline{\boldsymbol{M}}_h(\dot{\boldsymbol{x}}_j,\boldsymbol{x}_j)\ddot{\boldsymbol{x}}_i+\overline{\boldsymbol{C}}_h(\dot{\boldsymbol{x}}_j,\boldsymbol{x}_j)\dot{\boldsymbol{x}}_i+\overline{\boldsymbol{K}}_h(\boldsymbol{x}_j)\boldsymbol{x}_i=\boldsymbol{0}\quad\text{for } i,j=1,\ldots,N, \tag{107}$$

where the state vector is

$$\boldsymbol{x}_i=[\boldsymbol{\varphi}_i,\boldsymbol{\Theta}_i]^{\mathrm{T}} \tag{108}$$

and $\overline{\boldsymbol{M}}_h$, $\overline{\boldsymbol{C}}_h$ and $\overline{\boldsymbol{K}}_h$ are the semi-discretized system mass-, damping- and stiffness matrices, respectively. This form is well known in marine control engineering. In the simulations Matlab is applied, and the embedded ODE-solver `ode23tb` is used to solve the semi-discretized problem (107).

Table 1
Applied physical constants and parameters.

Parameter	Notation	Value	Unit
Constants			
Density of steel	ρ_s	7.850×10^6	kg/m^3
Density of water	ρ_w	1.025×10^3	kg/m^3
Acceleration of gravity	g	9.80665	m/s^2
Young's modulus steel	E	206×10^9	N/m^2
Shear modulus steel	G	7.9231×10^{10}	N/m^2
Pipe properties			
Outer pipe diameter	d_o	0.762	m
Wall thickness	WT	0.033	m
Undeformed pipe length	L	1500	m
Unit mass of empty pipe	m_p	593.2818	kg
Submerged unit weight	w_s	1.2341×10^3	N/m
Moments of inertia	I_1	78.9851	kg m^2
	$I_2=I_3$	39.4925	kg m^2
Unit polar moments of inertia	I	5.0309×10^{-3}	m^4
	J	1.0062×10^{-2}	m^4
Axial stiffness	EA	1.5569×10^{10}	N m^2
Shear stiffness	GA	9.0330×10^9	N m^2
Torsional stiffness	GJ	7.9720×10^8	N m^2
Bending stiffness	EI	1.0364×10^9	N m^2

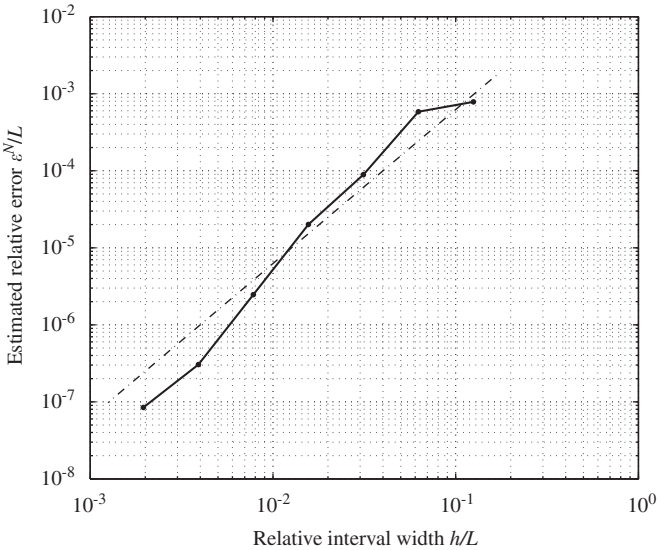

Fig. 3. The estimated relative error ε^N/L for the static solution approximations where the number of elements N-1 = 8, 16, 32, 64, 128, 256, 512, against relative interval width $h/L=1/(N\text{-}1)$, where an approximated solution with N-1 = 1024 is taken as the reference. The results compare well to the quadratic auxiliary line.

4.2. Scenario and parameters

For the analysis, we will consider the installing of a 30 in (0.762 m) OD (outer diameter) steel pipe, without weight coating, at a water depth of $h = 900$ m using the J-lay method, see Fig. 1. The seabed is assumed to be flat, there are no environmental disturbances, and the physical constants and material pipe properties applied in the analysis are listed in Table 1. This scenario and the parameters are chosen since they are realistic, and similar scenarios are analyzed for industrial applications.

The static analyses are performed in the vertical plane spanned by $\{\boldsymbol{e}_1, \boldsymbol{e}_3\}$ where different values for the horizontal tension

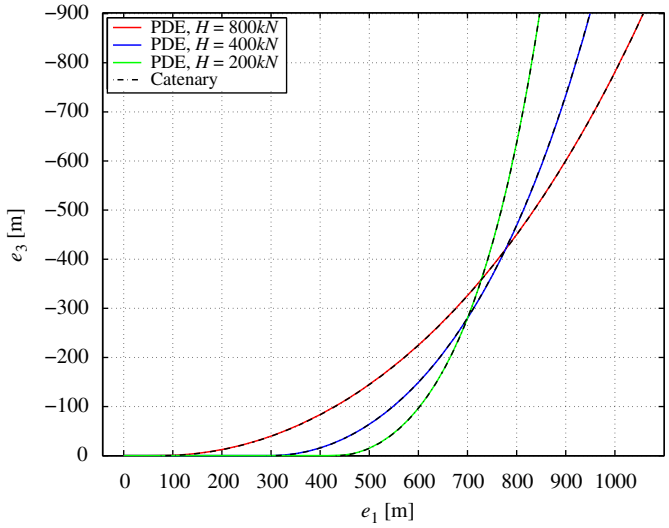

Fig. 4. Static pipe configuration without bending stiffness of the pipe model validated against the catenary.

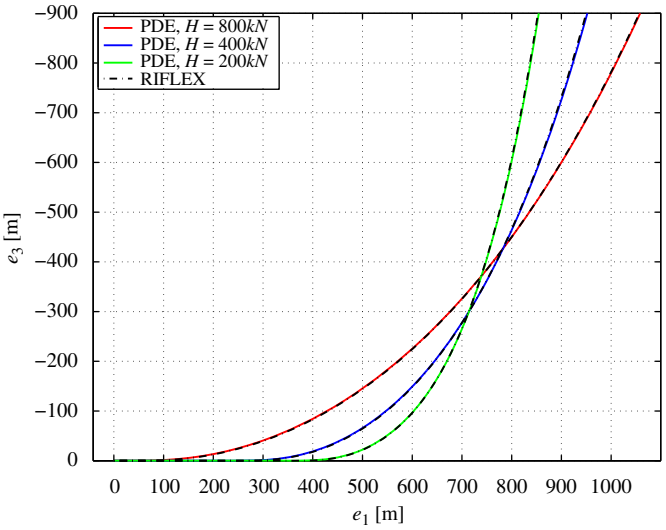

Fig. 6. Static pipe configuration of the pipe model validated against RIFLEX.

Table 2
Static analyses results for the pipe model without bending stiffness, e.g., $EI = 0$ and the catenary.

Horizontal tension	H	200	400	800	kN
Pipe model without bending stiffness, $EI = 0$					
Hang-off angle	β	81.22	74.64	65.24	deg
Lay-back distance	l_h	412.25	645.10	975.51	m
Catenary					
Hang-off angle	β	81.22	74.64	65.24	deg
Lay-back distance	l_h	415.25	649.41	982.24	m

Table 3
Static analyses results for the pipe model including the effects of bending stiffness and RIFLEX.

Horizontal tension	H	200	400	800	kN
Pipe model					
Hang-off angle	β	80.97	74.30	64.87	deg
Lay-back distance	l_h	467.92	679.76	996.29	m
RIFLEX					
Hang-off angle	β	81.0	74.4	65.0	deg
Lay-back distance	l_h	477	686	1001	m

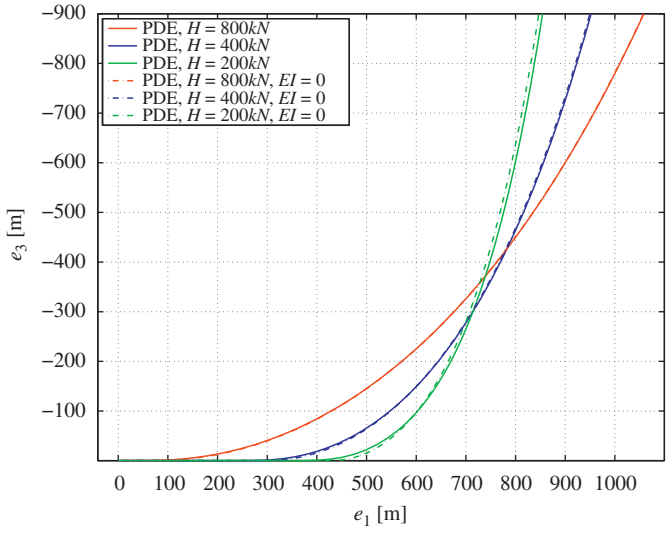

Fig. 5. Pipe model configurations with and without bending stiffness compared.

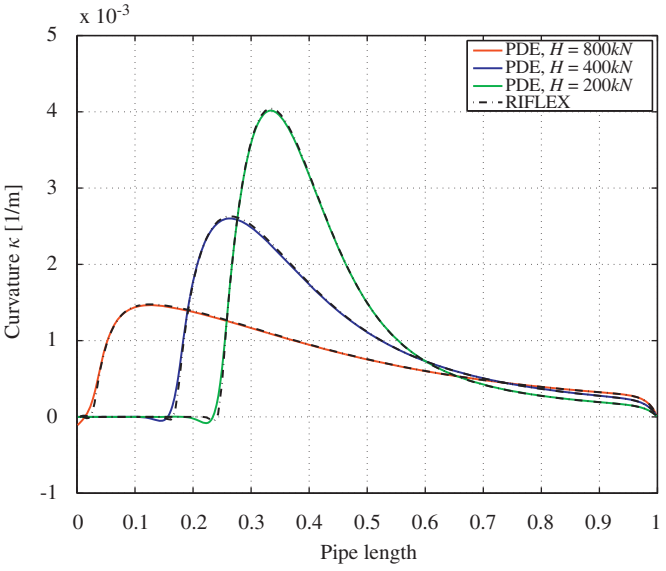

Fig. 7. Comparing the curvature κ of the pipe model and RIFLEX.

$H = \{200, 400, 800\}$ kN are applied to the top node at $\boldsymbol{\varphi}(L)$ in the $\boldsymbol{e}_1$−direction. In the dynamic analysis, the static configuration for $H = 400$ kN is assumed as the initial configuration. No lateral or axial seabed friction is assumed. The pipe at $S = 0$ is horizontally clamped to the seabed, and at $S = L$, it is attached to the center of gravity of the vessel, where it is free to rotate. A linearized vessel model is used where the coefficient matrices are obtained from the *marine systems simulator* (MSS) available at Fossen and Perez (2004). A DP system is implemented by a nonlinear PID controller, found in Jensen et al. (2009b), to force the surface vessel to track a circular path with period $T = 10$ s and diameter $\delta = 5$ m three times, before returning to its initial position, see Fig. 8. This imposes a spiraling motion on the pipe. The control reference is ramped to limit accelerations.

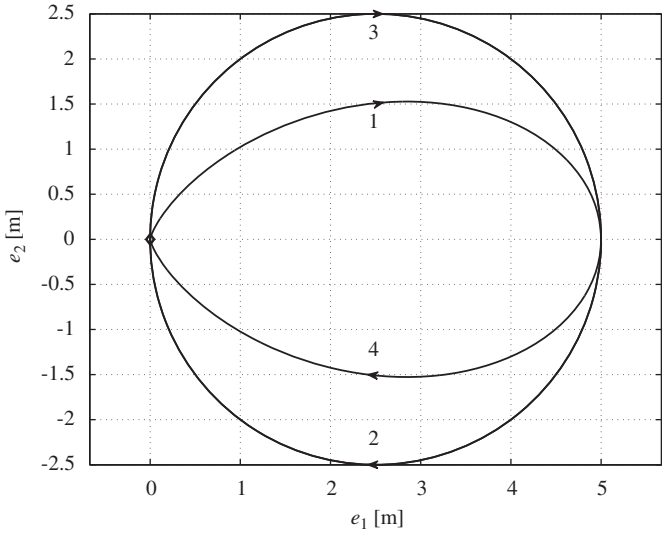

Fig. 8. The path followed by the surface vessel. The vessel starts in $(0, 0)$, which represents the surface position for the static solution where $H = 400$ kN. The path is made up of three complete circles with ramps to limit acceleration at the beginning and end. The sequence and direction is indicated by the arrows and numbers 1–4. After completing the third circle, the vessel remains fixed at $(0, 0)$.

The same number of nodes, with equal spacing are defined for the RIFLEX simulation. In addition, added mass and seabed friction are removed, and the vertical equilibrium for the pipe resting at the seabed is set to $d_o/2$, which is slightly below the corresponding equilibrium for the FEM simulation; $d_o/8$. The positions of the pipe tip over the course of 60 s of simulation with the FEM model is given as input to RIFLEX, as RIFLEX does not include the surface vessel dynamics.

4.3. Static solutions

To approximate the static solution, $G_{\text{stat}}(\boldsymbol{\varphi}, \boldsymbol{R}_t^e; \boldsymbol{u}, \boldsymbol{\vartheta}) = 0$, the Newton–Raphson strategy described in Simo and Vu-Quoc (1986) is applied. For the approximated static solution (97), let the averaged error estimate be given by

$$\varepsilon^N \triangleq \frac{1}{N}\sum_{i=1}^{N} \|(\boldsymbol{\varphi}_i, \boldsymbol{\Theta}_i) - (\boldsymbol{\varphi}^{\text{ref}}(S_i), \boldsymbol{\Theta}^{\text{ref}}(S_i))\|_2, \tag{109}$$

where the approximated solution from a fine gridded discretization is taken as a reference solution

$$(\boldsymbol{\varphi}^{\text{ref}}(S), \boldsymbol{\Theta}^{\text{ref}}(S)) \triangleq \sum_{i=1}^{N} (\boldsymbol{\varphi}_i, \boldsymbol{\Theta}_i) N_h^i(S). \tag{110}$$

The estimated convergence of ε^N is shown in Fig. 3.

The pipe model uses $N = 740$, such that element length is approximately 2 m. To validate the model against the catenary, the bending stiffness in the pipe model is set to zero, i.e., $EI = 0$, and the computed static configurations are plotted in Fig. 4,

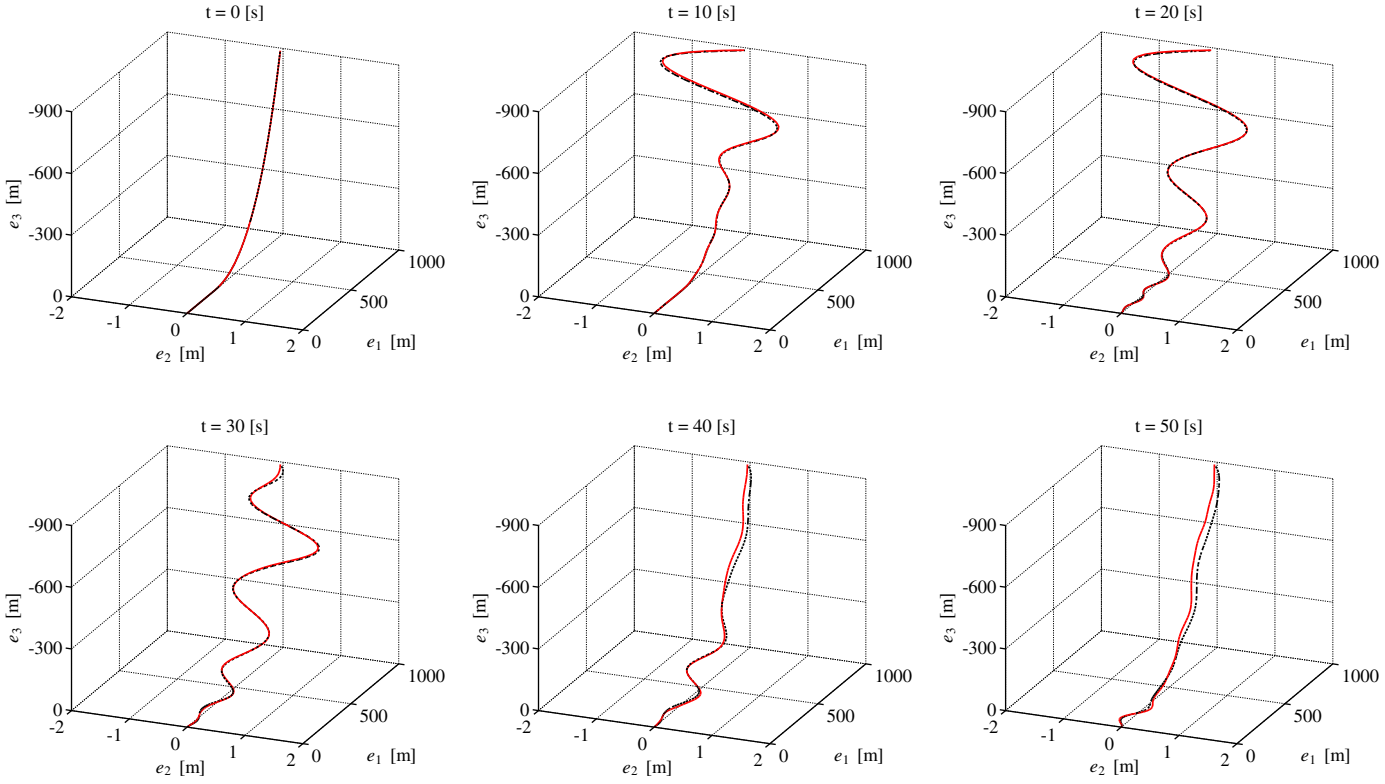

Fig. 9. Snapshots of the pipe configuration for the PDE model (red solid line), and RIFLEX (black dotted line) at $t = 0, 10, 20, 30, 40, 50$ s.

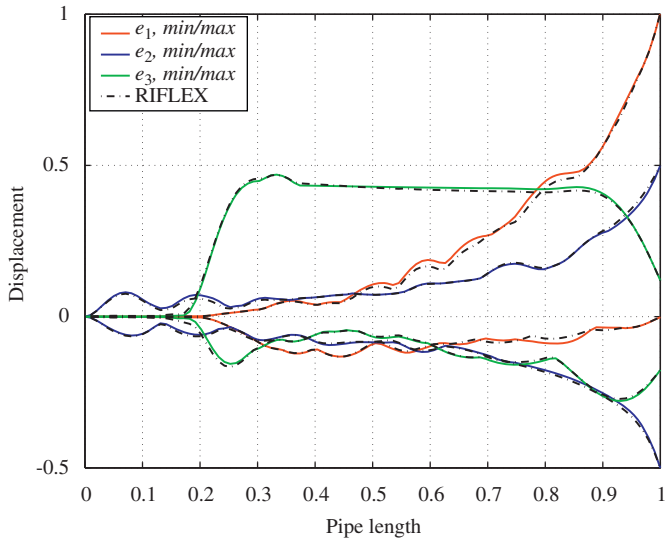

Fig. 10. Relative displacement envelope in the $\boldsymbol{e}_1$, $\boldsymbol{e}_2$ and $\boldsymbol{e}_3$ directions for the FEM model compared to RIFLEX.

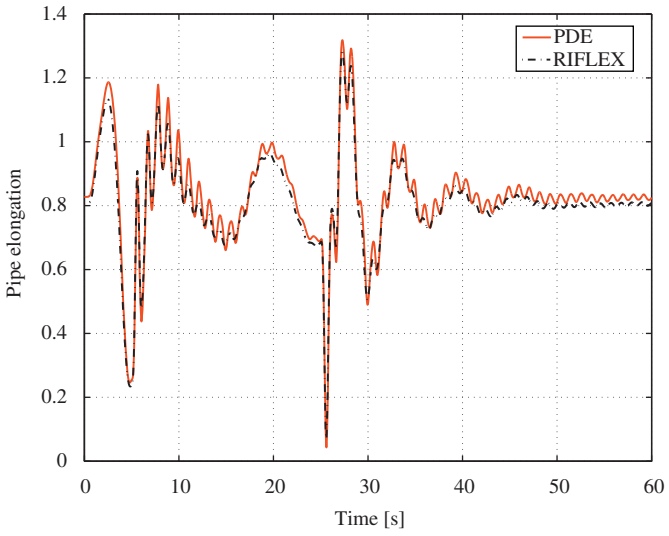

Fig. 11. Normalized total pipe length.

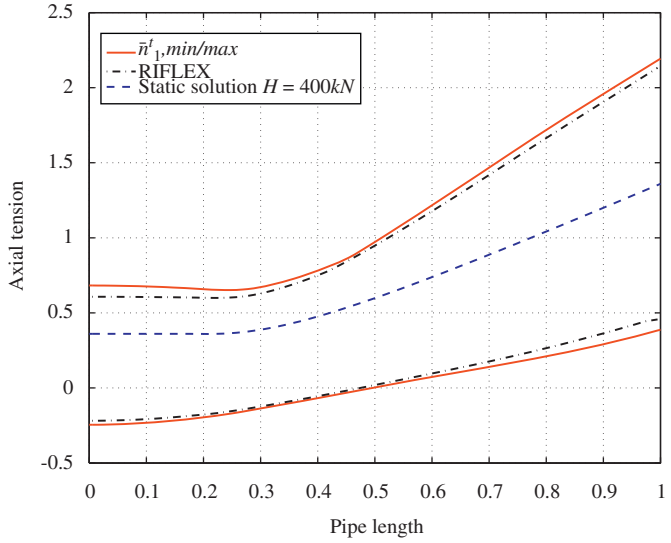

Fig. 12. Axial tension envelope, including the static axial tension for $H = 400$ kN.

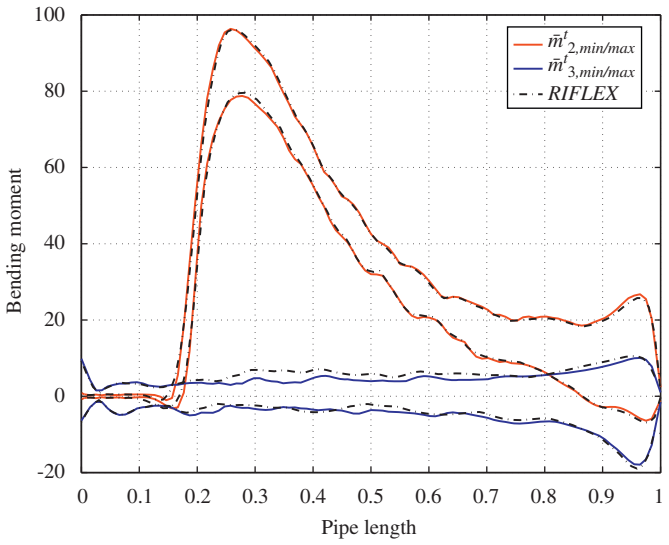

Fig. 13. Bending moment envelope about the $\boldsymbol{t}_2$ and the $\boldsymbol{t}_3$ axis along the pipe. This value is represented in the PDE by the min/max values for $\overline{m}^t_2$ and $\overline{m}^t_3$ along S. The results are compared to RIFLEX.

where the FEM model and the catenary configurations can hardly be distinguished. The hang-off angle β and the lay-back distance l_h, the horizontal distance from hang-off to touchdown, for the FEM and the catenary are presented in Table 2, and are seen to correspond well. The difference in lay-back distance differs with less than 0.7% from the catenary. This may be explained from the effect of the seabed interaction of the pipe model. Comparing the FEM model configuration with bending stiffness ($EI \neq 0$), and without ($EI = 0$), see Fig. 5, it is seen that the effect of the bending stiffness is most significant in the touchdown area and at the hang-off angle, and that it diminishes with increasing axial tension.

The computed static configurations including bending stiffness for the FEM model and RIFLEX are plotted in Fig. 6. The hang-off angles and lay-back distances are presented in Table 3, and corresponds well. The largest difference is found in the l_h, which for $H = 200$ kN is approximately 1.9%. As the tension increases, this difference decreases, $H = 400$ kN yields a relative error of 0.9%, and $H = 800$ kN yields a relative error of 0.5%. The curvature along the pipe configurations of Fig. 6 are plotted in Fig. 7, and show that the forces also correspond well in the two models (Fig. 8).

4.4. Dynamic simulations

In the dynamic simulation, $N = 100$ and the nodes are equidistant. The plots of the simulation results are divided in three groups; *geometric plots* (Figs. 9–11), *force and moment plots* (Figs. 12 and 13), and *node plots* (Fig. 14).

A snapshot of the pipe configuration is taken every 10 s over the course of the simulation, see Fig. 9. A wave propagates down the pipe and is reflected at the lower boundary, and the lack of longitudinal friction at the seabed can be seen. When the forced motion stops at $t = 30$ s, the hydrodynamic drag force are seen to damp out the pipe motion. The FEM and RIFLEX results are seen to follow closely. The nondimensional maximum relative displacement with respect to the vessel path diameter δ, from the initial

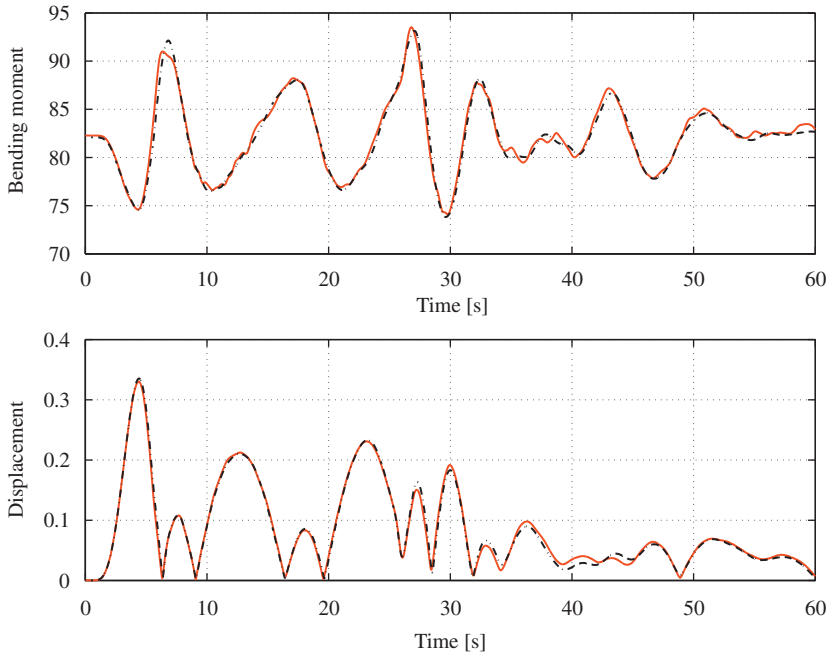

Fig. 14. Dynamic bending moment (top) and relative displacement (bottom) for a node ($N = 25$) close to the touchdown point.

configuration over the course of the simulation are compared in Fig. 10. Fig. 11 shows the pipe length relative to the length of a freely suspended pipe submerged in water, elongated only by its own weight.

The nondimensional maximum axial tension $\overline{n}_1^t$ over the course of the simulation is compared in Fig. 12. The axial tension along the axis $\boldsymbol{t}_1$ is given as the first component of the material stress resultant $\boldsymbol{n}^t$ (23), denoted n_1^t, and made nondimensional by $\overline{n}_1^t(S) = n_1^t(S)/(w_s h)$. The nondimensional maximum bending moments $\overline{m}_2^t$ and $\overline{m}_3^t$ along S are compared in Fig. 13. These are given by the stress couple $\boldsymbol{m}^t$ (24), along $\boldsymbol{t}_2$ and $\boldsymbol{t}_3$, where $\overline{m}_i^t(S) = m_i^t(S)/(w_s \delta^2)$, $i = 2, 3$. The largest values are found close to the touchdown and the surface vessel. The dynamic absolute displacement $\|\boldsymbol{\varphi}_{N=25}(t) - \boldsymbol{\varphi}_{N=25}(0)\|$ and bending moment, as functions of time for node $N = 25$, which is close to the touchdown point, is shown in Fig. 14.

By considering these analysis results, the nominal values correspond well, and the error between the FEM model and RIFLEX are not more than what can be expected from different numerical implementation.

4.5. Model convergence

For a practical applications of the numerical implementation, the convergence must be considered. The number of nodes in a simulation should be small to optimize computation time, while at the same time capture the main dynamic behavior of the system. The dynamic simulation scenario, given in the previous section, is repeated for $N = 10, 20, 40, 80$ nodes, and plotted against $N = 100$, used in the dynamic validation, see Fig. 15. Visually, the configurations of $N = 80$ and 100 cannot be distinguished, while the configuration for $N = 40$ can only be distinguished at some locations. For $N = 20$, the main dynamics are kept, while for $N = 10$, the oscillations differs much from that of $N = 100$. To improve the dynamics without increasing the number of nodes, variable element lengths can be introduced, such that sensitive regions along the pipe, i.e., the touchdown and the hang-off area, may have shorter elements than the less sensitive regions.

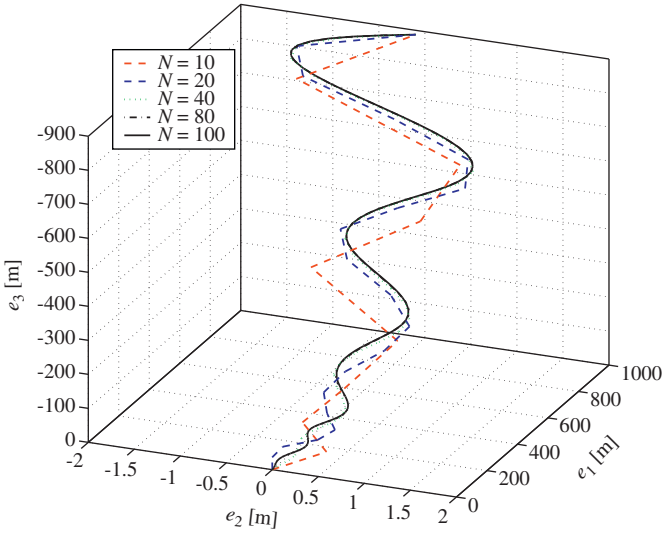

Fig. 15. Pipe configuration snapshot at $t = 15$ s for $N = 10, 20, 40, 80, 100$.

5. Conclusions

A dynamic model for a freely suspended pipe string with bending stiffness has been developed. This pipe model has been shown to be input–output passive by a passivity check. Further, the model has been extended to include the dynamics of a surface pipelay vessel, and passivity and stability of the combined system has been shown from considering the total energy of the system. The PDE pipe model has been semi-discretized into a FEM model, which has been implemented and successfully validated against the catenary equation and RIFLEX. This proves the validity of the PDE model, and that the FEM model can be used to analyze and simulate slender marine structures.

The advantage of this model over RIFLEX is that the discretization in space and time is performed in two separate steps. The semi-discretized PDE model is well suited for

simulating multibody systems, such as the pipe string and surface vessel scenario presented here, and may also be applied in observers. The range of analysis that can be performed using the proposed model extends that of RIFLEX, since the dynamics of the surface vessel is included in the model. Hence, it may be used to, e.g., analyze the interaction between a pipe string and a motion control systems for the surface vessel.

Future extensions to the model can be envisioned: adding lateral and longitudinal seabed friction, allow for uneven seabed by using bathymetry maps, allow pipe elongation my relaxing the fixed pipe length property so that $L = L(t)$. Converting to a parametrization of rotation with respect to quaternions rather than Euler angles will remove system singularities.

The numerical implementation in this paper was done in Matlab, using equidistant distributed nodes and built-in ODE solvers to integrate in time. The accuracy of the nominal values obtained in the simulation were very good, but real-time computation time could not be achieved. In order to improve the computation time, the ODE-solver should be replaced by a dedicated solver, e.g., by applying a geometric method (Hairer et al., 2002), which often achieve good stability properties and good behavior in long-time simulations, and by implementing the discretized model in a more suited compilable language (Säfström, 2009).

Acknowledgments

The authors wish to thank Mr. Dag Fergestad of MARINTEK for providing the RIFLEX data used for model validation, Professor Carl Martin Larsen of the Department of Marine Technology, and Associate Professor Elena Celledoni of the Department of Mathematical Sciences, both at NTNU, for fruitful discussions. The authors also wish to thank Dr. Yilmaz Türkyilmaz who's initial work on the model presented here has benefited the authors. This work has partially been supported by the Norwegian Research Council (NFR) through the Centre for Ships and Ocean Structures (CeSOS) at the NTNU and through the strategic university program (SUP) on Computational Methods in Nonlinear Motion Control (CMinMC).

References

Åström, K.J., 1996. Automatic control: a perspective. Colloquium on automatic control. Lecture Notes in Control and Information Sciences, vol. 215. Springer, Berlin, Heidelberg, pp. 1–26.

Balas, M.J., 1978. Active control of flexible systems. Journal of Optimization Theory And Applications 25 (3), 415–436.

Betsch, P., Steinmann, P., 2002. Frame-indifferent beam finite elements based upon the geometrically exact beam theory. International Journal for Numerical Methods in Engineering 54 (12), 1775–1788.

Braestrup, M.W., Andersen, J.B., Andersen, L.W., Bryndum, M.B., Christensen, C.J., Rishøy, N., 2005. Design and Installation of Marine Pipelines. Blackwell Science Ltd.

Dixon, D., Rutledge, D., 1968. Stiffened catenary calculations in pipeline laying problem. ASME Journal of Engineering for Industry 90, 153–160.

Egeland, O., Gravdahl, J.T., 2002. Modeling and Simulation for Automatic Control, first ed. Marine Cybernetics, Trondheim, Norway.

Faltinsen, O.M., 1990. Sea Loads on Ships and Offshore Structures. Cambridge University Press, Cambridge.

Fathi, D., 2004. ShipX Vessel Responses (VERES). MARINTEK, Trondheim ⟨www.marintek.sintef.no⟩.

Fossen, T.I., 2002. Marine Control Systems: Guidance, Navigation, and Control of Ships, Rigs and Underwater Vehicles, first ed. Marine Cybernetics, Trondheim Norway.

Fossen, T.I., Perez, T., 2004. Marine systems simulator (MSS) ⟨www.marinecontrol.org⟩.

Fossen, T.I., Smogeli, Ø.N., 2004. Nonlinear time-domain strip theory formulation for low-speed manoeuvering and station-keeping. Modeling, Identification and Control 25 (4), 201–221.

Fylling, I., Larsen, C.M., Sødahl, N., Passano, E., Bech, A., Engseth, A.G., Lie, H., Ormberg, H., 2008. RIFLEX User's Manual 3.6. MARINTEK, Trondheim, Norway.

Guo, B., Song, S., Chacko, J., Ghalambor, A., 2005. Offshore Pipelines. Gulf Professional Publishing.

Hairer, E., Lubich, C., Wanner, G., 2002. Geometric numerical integration. Springer Series in Computational Mathematics, vol. 31. Springer, Berlin.

Heerema, E., 2005. Recent achievements and present trends in deepwater pipe-lay systems. In: Proceedings of the 37th Offshore Technology Conference, OTC 17627.

Irvine, H.M., 1981. Cable Structures. MIT Press, Cambridge, MA.

Jensen, G.A., Breivik, M., Fossen, T.I., 2009a. Offshore pipelay operations from a control perspective. In: Proceedings of the 28th OMAE, Honolulu, Hawaii, USA.

Jensen, G.A., Säfström, N., Nguyen, T.D., Fossen, T.I., 2009b. Modeling and control of offshore pipelay operations based on a finite strain pipe model. In: Proceedings of the 2009 American Control Conference, St. Louis, USA.

Khalil, H., 2002. Nonlinear Systems, third ed. Prentice-Hall, Englewood Cliffs, NJ.

Love, A.E.H., 1944. The Mathematical Theory of Elasticity. Dover, New York.

Martinsen, M., 1998. A finite element model for pipeline installation. Master's Thesis, Stavanger University College for JP Kenny A/S.

McRobie, F., Lasenby, J., 1999. Simo–Vu Quoc rods using Clifford algebra. International Journal for Numerical Methods in Engineering 45 (4), 377–398.

Morison, J.R., O'Brien, M.P., Johnson, J.W., Schaaf, S.A., 1950. The force exerted by surface waves on piles. Petroleum Transactions AIME 189, 149–189.

Ogilvie, T.F., 1964. Recent progress toward the understanding and prediction of ship motions. In: Proceedings of the 5th Symposium on Naval Hydrodynamics, vol. ACR-112. Bergen, Norway. ONR, pp. 3–79.

Palmer, A.C., King, R.A., 2008. Subsea Pipeline Engineering, second ed. PennWell Books.

Perez, T., Fossen, T.I., 2007. Kinematic models for manoeuvring and seakeeping of marine vessels. Modeling, Identification and Control 28 (1), 19–30.

Plunkett, R., 1967. Static bending stresses in catenaries and drill strings. ASME Journal of Engineering for Industry 89, 31–36.

Reissner, E., 1982. Some remarks on the problem of column buckling. Ingenieur Archiv 52, 115–119.

Romero, I., Armero, F., 2002. An objective finite element approximation of the kinematics of geometrically exact rods and its use in the formulation of an energy-momentum conserving scheme in dynamics. International Journal for Numerical Methods in Engineering 54 (12), 1683–1716.

Säfström, N., Modeling and simulation of rigid body and rod dynamics via geometric methods, Ph.D. thesis of Norwegian University of Science and Technology 2009;247, ISBN 978-82-471-1906-8 (Electronic version).

Sciavicco, L., Siciliano, B., 2001. Modelling and Control of Robot Manipulators, second ed. Springer, Berlin.

Simo, J.C., 1985. A finite strain beam formulation. The three-dimensional dynamic problem. Part I. Computer Methods in Applied Mechanics and Engineering 49 (1), 55–70.

Simo, J.C., Tarnow, N., Doblare, M., 1995. Non-linear dynamics of three-dimensional rods: exact energy and momentum conserving algorithms. International Journal For Numerical Methods in Engineering 38, 1431–1473.

Simo, J.C., Vu-Quoc, L., 1986. A three-dimensional finite-strain rod model. Part II: computational aspects. Computer Methods in Applied Mechanics and Engineering 58 (1), 79–116.

Simo, J.C., Vu-Quoc, L., 1988. On the dynamics in space of rods undergoing large motions—a geometrically exact approach. Computer Methods in Applied Mechanics and Engineering 66 (2), 125–161.

SNAME, 1950. Nomenclature for treating the motion of a submerged body through a fluid. Technical and Research Bulletin No. 1–5.

WAMIT, 2004. WAMIT User Manual ⟨www.wamit.com⟩.